# Neural network retrieval of cloud parameters of inhomogeneous clouds from multispectral and multiscale radiance data: Feasibility study

Céline Cornet,[1] Harumi Isaka, Bernard Guillemet, and Frédéric Szczap

Laboratoire de Météorologie Physique, UMR/CNRS, Observatoire de Physique du Globe de Clermont-Ferrand, Université Blaise Pascal, Clermont-Ferrand, France

[1] In this paper, we investigated the feasibility of retrieving cloud parameters of inhomogeneous and fractional clouds from simulated multispectral and multiscale radiometric data by using mapping neural networks. A radiometric database prepared for neural network training consists of area-averaged radiance data for two pixel scales, i.e., (1 km × 1 km) and (0.25 km × 0.25 km) pixels, respectively. The cloud parameter retrieval assumes a vertically uniform inhomogeneous and fractional cloud defined with 6 parameters, i.e., the mean and standard deviation of optical thickness, the mean and standard deviation of effective radius, the fractional cloud cover, and the cloud top temperature, all defined at a scale of cloud parameter retrieval. The retrieval procedure comprises two separate steps: the first one is relative to the angular interpolation and correction of radiance data (surface reflection and thermal emission contribution). The second step concerns the cloud parameter retrieval as such from interpolated and corrected radiance data. The input vector to the retrieval MNNs consists of 8 radiometric data in addition to a number of necessary ancillary data such as surface temperature and ground albedo. The 8 radiometric data are 5 area-averaged radiances over (1 km × 1 km) pixel and 3 standard deviations of radiance over (1 km × 1 km) pixel estimated from (0.25 km × 0.25 km) pixel radiances. After evaluating the performance of the neural networks trained for each step, we tested the whole retrieval procedure for three types of inhomogeneous and fractional clouds: flat-top bounded cascade clouds and flat-top and non-flat-top Gaussian process clouds. All the cloud parameters of these clouds can be retrieved with reasonable accuracy in spite of the fact that the mean and standard deviation of optical thickness of non-flat-top clouds exhibit some dispersion. The inclusion of (0.25 km × 0.25 km) pixel radiance data as input vector components improved significantly the performance of the cloud parameter retrieval. Finally, we analyzed the consequences of some simplifying assumptions on the retrieved cloud parameters, and discussed the perspectives of the cloud parameter retrieval based on the neural networks.    INDEX TERMS: 0320 Atmospheric Composition and Structure: Cloud physics and chemistry; 3260 Mathematical Geophysics: Inverse theory; 3360 Meteorology and Atmospheric Dynamics: Remote sensing; 3359 Meteorology and Atmospheric Dynamics: Radiative processes; KEYWORDS: cloud retrieval, inhomogeneity, neural network

Citation: Cornet, C., H. Isaka, B. Guillemet, and F. Szczap (2004), Neural network retrieval of cloud parameters of inhomogeneous clouds from multispectral and multiscale radiance data: Feasibility study, J. Geophys. Res., 109, D12203, doi:10.1029/2003JD004186.

## 1. Introduction

[2] In recent years, various methods have been proposed to retrieve cloud parameters from multispectral radiance data under the plane-parallel homogeneous cloud assumption [Nakajima and King, 1990; Nakajima et al., 1991; Nakajima and Nakajima, 1995; Platnick and Valero, 1995]. As far as informative radiance data are limited to two wavelengths (one in visible and the other in near infrared), one can consider only an inverse cloud model with two cloud parameters. However, there is some degree of freedom in the choice of cloud parameters to retrieve; Brenguier et al. [2000] retrieved the cloud depth and droplet number concentration under adiabatic droplet growth assumption instead of the usual optical thickness and effective radius.

[3] When inhomogeneous clouds are treated as homogeneous clouds, the variability of microphysical parame-

---

[1] Also at Laboratoire d'Optique Atmosphérique, Université des Sciences et Technologies de Lille, Villeneuve d'Ascq, France.

ters at scales smaller than averaging scale leads to biases in radiance and radiative flux, which is called 'plane-parallel bias' [*Cahalan et al.*, 1994b; *Loeb et al.*, 1997; *Oreopoulos and Davies*, 1998; *Szczap et al.*, 2000a]. The plane-parallel bias also varies significantly with the scale of averaging [*Davis et al.*, 1997; *Oreopoulos et al.*, 2000a]. Hence, when the optical thickness and effective radius of inhomogeneous clouds are retrieved under the plane-parallel homogeneous cloud assumption, the retrieved values only represent their corresponding 'effective' values, which are a function of the sub-pixel cloud heterogeneity and differ significantly from their means over observation pixel [*Szczap et al.*, 2000a].

[4] There have been some attempts to retrieve cloud parameters, in particular optical thickness, of inhomogeneous clouds [*Chambers et al.*, 1997; *Marshak et al.*, 1998; *Oreopoulos et al.*, 2000b; *Cahalan et al.*, 2001] and to evaluate the effect of small scale variability on the retrieved cloud parameters [*Davis et al.*, 1997; *Iwabuchi and Hayasaka*, 2002; *Varnai and Marshak*, 2001, 2002]. Recently, *Faure et al.* [2001a, 2002, referred to hereinafter as FIG01 and FIG02, respectively] showed the feasibility of retrieving cloud parameters (mean optical thickness, effective radius, fractional cloud cover and sub-pixel scale cloud inhomogeneity) of horizontally inhomogeneous clouds, by using mapping neural network (abbreviated hereafter as MNN). They also showed that an MNN retrieval algorithm could integrate easily radiances of neighbor pixels as additional input data and retrieve the cloud parameters even if the size of observation pixel is too small to neglect the horizontal photon transport to and from neighbor pixels (FIG01, FIG02). This enables us to bypass an implicit assumption that neighbor pixels do not influence the radiance from an observation pixel, i.e., the pixel is large enough so that one might neglect effects of horizontal photon transport between a target pixel and its neighbors.

[5] Compared to Advanced Very High Resolution Radiometer (AVHRR), new space-borne radiometers such as MODIS (Moderate Resolution Imaging Spectroradiometer) on TERRA or GLI (Global Imager) on ADEOS 2 have more spectral channels in near infrared and measure radiance averaged over a pixel of smaller size; GLI/ADEOS 2 has also multiscale measurement capability. Their data are also accompanied by other collocated radiometric data: multidirectional radiance data (MISR/TERRA and POLDER/ADEOS 2) or microwave radiance data (AMSR/ADEOS 2). This raises a question how one can use these better observation capabilities to improve retrieval algorithms, i.e., to retrieve more pertinent cloud parameters that are compatible with available radiometric data, by taking into account of more realistic cloud characteristics.

[6] The first objective of the present study is to extend the work started in FIG01 to more realistic conditions of the cloud parameter retrieval and to confirm that the MNN retrieval of cloud parameters is effectively feasible by using radiance data. In doing so, we have to solve some technical problems that have been left unexplored in FIG01. The first problem is relative to the interpolation of radiance data from an arbitrary solar incidence-viewing configuration to the nearest MNN solar incidence-viewing configuration (abbreviated hereafter MNN I-V configuration) for which a cloud parameter retrieval MNN is trained. The second problem is

relative to decoupling radiance due to the cloud layer reflection from other undesirable components such as those reflected by underlying earth surface or emitted by both cloud layer and underlying earth surface.

[7] The second objective is to investigate the impact of multiscale radiometric data to the cloud parameter retrieval. In fact, the usual cloud parameter retrieval uses only area-averaged multispectral radiance data. In the present study, we investigate the impact of multispectral radiance data measured at a smaller pixel (0.25 km × 0.25 km) to the cloud parameter retrieval at a larger pixel (1 km × 1 km). A sensitivity study such as the one presented in this paper would be useful to analyze what kinds of cloud parameters are best to be retrieved from available radiometric data and/or what kinds of radiance data are more pertinent for planned cloud parameter retrieval.

[8] The outline of the present paper is as follows. In section 2, we discuss general principles of the cloud parameter retrieval and explain the reason why our retrieval procedure is based on the application of MNNs. In section 3, we describe briefly characteristics of radiance database we have prepared for the present study. In section 4, we present the generalization performance of MNNs we trained for each step of the retrieval procedure. We will discuss also the difference between cloud parameters retrieved for two types of inverse cloud models, the one with the inhomogeneous clouds and the other with the plan-parallel homogeneous clouds. In section 5, we will assess the overall performance of the retrieval procedure by applying it to flat-top bounded cascade clouds and flat-top and non-flat-top Gaussian process clouds. Finally, we will discuss perspectives of the cloud retrieval procedure based on the application of MNNs in section 6.

## 2. Retrieval Algorithm
### 2.1. Principles of Cloud Parameter Retrieval

[9] Neural networks are increasingly applied to data inversion because they are well adapted to find non-linear statistical relationships between target variables and input variables [*Faure et al.*, 2001a; *Krasnopolsky and Schiller*, 2003]. They can be used as "black box model" providing only effective target-input mapping between observed target and input variables [*Harris et al.*, 1998]. However, one should be very cautious about such 'black box' application of the MNN for the cloud parameter retrieval. A critical issue is whether such a statistical model can provide sufficient insight into underlying physical processes that generated the training data; examples of such utilization of MNNs were given by *Faure et al.* [2001b, 2001c].

[10] The rationale why the present retrieval algorithm uses an MNN approach is that an MNN or other statistical approach is inherently required to deal with the retrieval of cloud parameters of inhomogeneous and fractional clouds. Once an inverse cloud model and its characteristic parameters are defined for the cloud parameter retrieval, one of the following two cases occurs. In the first case, the inverse cloud model can be used as 'direct cloud model' with prescribed cloud parameters for radiance field simulation, as with the plan-parallel homogeneous cloud model. In this case, one can solve the inverse problem by using classical methods of parameter optimization or more practically by
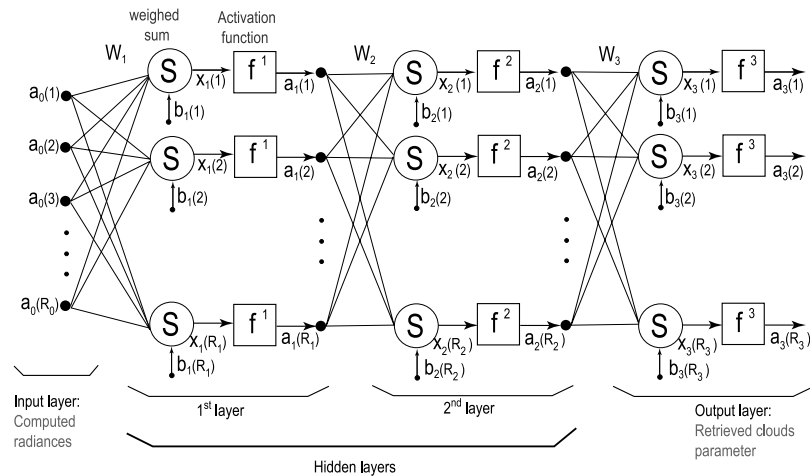
**Figure 1.**   Schematic description of feed-forward neural network architecture.

using look-up tables. In the second case, one cannot use the inverse cloud model as 'direct cloud model' for radiance field simulation by some reasons. This situation actually happens for inhomogeneous clouds, because we have no adequate method to generate an inhomogeneous cloud scene at observation pixel scale with a set of prescribed cloud parameters and to compute corresponding radiance fields. Consequently, we simulated radiance field of an inhomogeneous cloud scene with variable cloud parameters in the following way. In the first step, we generated an inhomogeneous cloud scene for a large cloud domain (6.4 km × 6.4 km domain in our case), much larger than the observation pixel, and simulated radiance fields for this large cloud domain. In the second step, we computed area-averaged radiances and corresponding variances as well as area-averaged cloud parameters for observation pixels (1 km × 1 km pixels in our case), which were randomly sampled within the above large cloud domain. This way of generating radiance data excludes totally the definition of 'direct cloud model' at the scale of observation pixel, and consequently the parameter optimization or look-up table approach.

[11]  We need to discuss briefly the problem of relationships between cloud parameters of an inverse cloud model (target vector) and available radiance and ancillary data (input vector). An inverse cloud model is usually defined as a compromise between the available radiance data and their supposed information content on the one hand and the attempt to retrieve as many independent and pertinent cloud parameters as possible on the other hand. The cloud parameter retrieval relies implicitly on a basic assumption that there is a one-to-one correspondence between the target vectors and input vectors. However, this basic assumption is not verified in all over the input vector space even for the simple plane-parallel homogenous cloud model, because two different sets of cloud parameters may correspond to the same set of radiance measured at two wavelengths in some part of the input vector space. Compared with the plane-parallel homogeneous inverse cloud with 2 cloud parameters, the situation may be worse for inhomogeneous clouds whose inverse cloud requires more than 2 cloud parameters and a large number of input vector components.

[12]  The inverse cloud used in this study is a cloud with vertically uniform microphysical and optical properties, and

it is defined with 6 cloud parameters: mean optical thickness ($\bar{\tau}_p$), mean effective radius ($\bar{r}_p$), standard deviation of optical thickness ($\sigma_{\tau,p}$), standard deviation of effective radius ($\sigma_{r,p}$), fractional cloud cover ($\bar{f}_p$), and cloud top temperature ($\bar{T}_p$). Theses cloud parameters have been defined by assuming that the effect of exact spatial distribution of fluctuations within an observation pixel can be neglected as first order approximation [Szczap et al., 2000a, 2000b]. For such an inverse cloud, the one-to-one correspondence between target vectors and input vectors is only an approximate one with inherent dispersions as shown in FIG01. It would be also very difficult, from the practical point of view, to ascertain that multiple solutions do not occur in such approximate one-to-one correspondence between target vectors and input vectors.

## 2.2.   Brief Description of the MNN

[13]  An MNN is an example of basis function models having a remarkable flexibility to approximate a multivariate function without knowing exactly its form [Hecht-Nielsen, 1990; Denison et al., 2002]. Figure 1 represents the general architecture of multiple-layer MNN with $L$ hidden layers. The input layer, numbered as 0th layer, does not contain any real neuron because its role only is to spread the input vector components to hidden cells in the 1st hidden layer. The hidden layers numbered $k = 1,\ldots, L$ are characterized by their weight matrices $\mathbf{W}_k$, bias vectors $\mathbf{b}_k$, and corresponding output vectors $\mathbf{a}_k$; the $(L + 1)$th layer is the output layer. Each hidden layer contains a number of hidden cells $N_k$. The relation between input and output vectors of the kth layer is expressed by

$$\mathbf{a}_k = f_k(\mathbf{x}_k) \text{ with } \mathbf{x}_k = \mathbf{W}_k\mathbf{a}_{k-1} + \mathbf{b}_k \qquad (1)$$

where $f_k$ is called 'transfer function' or 'basis function' of the kth layer. Hierarchies of 'hidden layers' are often constructed by using sigmoidal basis functions up to the last layer to which a linear model or linear transformation is usually fitted. A training data set is composed of a number of patterns; a pattern associates a target scalar or vector and input vector ($\mathbf{t}_l, \mathbf{a}_{0,l}$) with $l = 1,\ldots, M$, where $M$ is the size of training data set. A back-propagation scheme enables to estimate the weight matrices $\mathbf{W}_k$ and bias vectors $\mathbf{b}_k$ by

minimizing a cost function; the square error is usually adopted as cost function:

$$E = \sum_{l=1}^{M} \left(\mathbf{a}_{L,l} - \mathbf{t}_l\right)^t \cdot \left(\mathbf{a}_{L,l} - \mathbf{t}_l\right). \quad (2)$$

[14] One of the drawbacks of MNN function approximation is 'over-training' or 'over-fitting', which results in poor generalization ability. Another drawback is that there is no method to select 'a priori' an optimal structure of MNN adapted to the available target and input vectors. We have to be careful with errors induced by learning uncertainties in weight vectors and by intrinsic noise on the target vectors [*Penny et al.*, 1999]. The Bayesian approach to neural network training has provided some remedy to these problems [*MacKay*, 1992; *Neal*, 1996]. Indeed, MacKay's Bayesian approach contains a natural penalty against complex models, so-called Occam's razor, which states that a simpler model is favored over a more complex one, all other things being equal [*Denison et al.*, 2002].

[15] After testing different MNN structures, we selected a feed-forward MNN with 7 hidden cells in the first layer, 5 hidden cells in the second layer and 1 or 2 output cells in the third layer. The basis functions are tangent hyperbolic for the 1st and 2nd layers and the linear transformation in the 3rd layer for most of retrieval and prediction tasks in this study. We have trained all the MNNs by using the Levenberg-Marquardt algorithm for the back-propagation with Bayesian regularization in the MATLAB neural network toolbox. Compared with other training schemes, this scheme can improve significantly the generalization ability of the MNNs.

## 3. Radiance Database and MNN Training Data Sets

### 3.1. Radiative Transfer Code

[16] Radiance fields of inhomogeneous clouds were computed with SHDOM [*Evans*, 1998]. In its original version, it takes into account of atmospheric effects for spectral broadbands defined by *Fu and Liou* [1992]. However, to generate radiance data used for cloud parameter retrieval, we need radiance fields computed for narrow bands. For this purpose, the atmospherics part of *Nakajima and Nakajima*'s code [1995] has been implemented in SHDOM; the absorption coefficients are interpolated for $O_2$, $CO$, $N_2O$, $NH_3$, $NO$, $NO_2$, $SO_2$, $N_2$ and $CH_4$ from LOWTRAN7 database [*Kneizys et al.*, 1988]. US standard atmosphere is used for the temperature profile. To validate the 'modified SHDOM', we compared it with Nakajima and Nakajima's code for homogeneous clouds and with MYSTIC [*Mayer*, 1999] for inhomogeneous clouds respectively. The comparison has been done for a visible wavelength (0.67 μm) and for a thermal wavelength (11 μm); the 'modified SHDOM' was found to agree with the other codes within ±2% except for viewing directions close to horizontal plane.

### 3.2. Generation of Inhomogeneous Clouds With Fractional Cloud Cover

[17] To prepare a radiance database for the MNN training, we have to decide what cloud model to be used to generate inhomogeneous cloud scenes. It should have microphysical, structural and statistical characteristics as similar as possible to those of natural clouds. *Cahalan et al.* [1994a] proposed a 1D bounded cascade cloud to model measured fluctuations of liquid water path, and *Marshak et al.* [1995] extended the bounded cascade cloud model to 2D case. *Loeb et al.* [1998] and *Iwabuchi* [2000] used a stochastic cloud model based on the Gaussian process, which generates cloud scenes without a 'un-natural' appearance of bounded cascade clouds. However, there is no experimental data to validate statistical characteristics generated by a Gaussian stochastic cloud. More recently, *Roux et al.* [2000] have developed a cloud model based on wavelet decomposition of natural cloud scenes and subsequent recomposition by respecting their statistical characteristics. *Benassi et al.* [2004] also have proposed the tdMAP cloud model (tree-driven Mass Accumulation Process) based on a tree structure where different items (function, random variable, to shift branch, 'pruning'..) are applied at each node. However, one needs more detailed analysis before one can use these new cloud models for the preparation of radiance database. Hence, we decided to adopt the bounded cascade clouds. The rationale for this choice is an implicit assumption that the exact nature of 'direct' inhomogeneous cloud models is not important as far as the inhomogeneous clouds can be characterized by the first and second order moments of sub-pixel scale fluctuations of cloud parameters. From this point of view, it is better to select the bounded cascade clouds, which allow a wide range of variability of cloud parameters. We generated the fractional cloud cover by the same method as in FIG01.

[18] *Nakajima and Nakajima* [1995] and *Han et al.* [1998] showed that liquid water clouds over ocean exhibited some degree of correlation between effective radius and optical thickness, which varies from one cloud scene to another. Assuming that such a correlation exists also at sub-pixel scales, we generated fluctuations of effective radius and optical thickness at sub-pixel scales by using the same technique as in FIG02.

### 3.3. Preparation of Radiance Database of Inhomogeneous and Fractional Clouds

[19] Bounded cascade clouds were generated for a domain of 6.4 km × 6.4 km. This cloud domain is composed of 128 × 128 elementary cells of 50 m × 50 m in horizontal extension. The parameters H, $p_1$ and $p_2$ of the bounded cascade model are set equal to 1/3, 0.26 and 0.34 respectively, which corresponds approximately to −5/3 spectral slope of variable fluctuations. The effective radius is computed by assuming a lognormal droplet size distribution with a constant standard deviation of 0.35 [*Nakajima and Nakajima*, 1995].

[20] The present radiance database contains 6.4 km × 6.4 km inhomogeneous cloud scenes generated for four different sets of 'cloud-domain-mean' optical thickness $\tilde{\tau}_D$, 'cloud-domain-mean' effective radius $\tilde{r}_D$ and 'cloud-domain' fractional cover $\tilde{f}_D$ (Table 1). The 'pixel-mean' optical thickness $\bar{\tau}_p$, 'pixel-mean' effective radius $\bar{r}_p$, standard deviation of optical thickness $\sigma_{\tau,p}$, standard deviation of effective radius $\sigma_{r,p}$, fractional cloud cover $\bar{f}_p$ and cloud top temperature $\bar{T}_p$ are estimated for randomly selected (1 km × 1 km) observation pixels. The cloud top temperature $\bar{T}_p$ represents the mean cloud top temperature within

**Table 1.** Characteristics of the Cloud Domains Used for Radiance Simulation[a]

| $\tilde{\tau}_D$ | $\tilde{r}_D$, μm | $\tilde{f}_D$ | $\tilde{\Gamma}_D$ |
|---|---|---|---|
| 5 | 10 | 0.8 | 0.70 |
| 10 | 12 | 0.8 | 0.69 |
| 12 | 10 | 0.6 | 0.84 |
| 15 | 20 | 0.6 | 0.82 |

[a]$\tilde{\tau}_D$, mean optical thickness over cloud domain; $\tilde{r}_D$, mean effective radius over cloud domain; $\tilde{f}_D$, fractional cloud cover over cloud domain; $\tilde{\Gamma}_d$, correlation coefficient between $\tilde{\tau}_D$ and $\tilde{r}_D$ estimated over cloud domain.

an observation pixel. The standard deviation estimated over the observation pixel represents the sub-pixel cloud inhomogeneity. We did not normalize the standard deviation by the corresponding mean, because such a normalized inhomogeneity parameter becomes too large for small pixel-mean optical thickness or effective radius, which deteriorates considerably the MNN training. The cloud parameters estimated for (1 km × 1 km) pixels vary from 0 to 40 for optical thickness, from 0 to 27 μm for effective radius, from 0 to 23 for standard deviation of optical thickness, from 0 to 13 μm for standard deviation of effective radius, and from 0 (cloud free pixel) to 1 (overcast pixel) for fractional cloud cover respectively. The ranges of variation of 'pixel-mean' optical thickness and effective radius are similar to those observed by *Nakajima and Nakajima* [1995]. However, these ranges of variation might be too limited to cover all naturally possible range of cloud parameters and environmental conditions.

[21] In addition to the microphysical and optical characteristics and their horizontal inhomogeneity, we have to consider, in principle, different cloud base heights and geometrical cloud depths. For the homogeneous clouds, we do not need to consider such variations at least for visible and near infrared wavelengths, because their radiance fields depend mostly on the cloud optical thickness and not on the geometrical cloud depth. The situation differs significantly for the inhomogeneous and fractional clouds. In fact, the horizontal distribution of cloud shadows and 'hot spots' on earth surface changes as the cloud base height and/or geometrical cloud depth changes even if its horizontal distribution of inhomogeneity remains unchanged. Hence, the area-averaged radiance of the same observation pixel may vary significantly with the variation of cloud base height and/or depth. We evaluated the effect of the cloud base height and geometrical cloud depth on the area-averaged radiance for flat-top clouds, by simulating radiance fields of an identical inhomogeneous cloud scene over an underlying earth surface with small albedos of 0.05 and 0.1 (cf. Appendix A).

[22] Based on the results of this test, we have assumed, as first order approximation, that the cloud base height and geometrical cloud depth have only minor effect on the radiance fields of GLI-channel Nos. 8, 28, and 29. This assumption allows us to use only one geometrical cloud characteristics for these wavelengths, i.e., a cloud base height of 0.5 km and a cloud depth of 0.3 km, which are typical geometrical characteristics of low-level stratiform clouds. As for GLI-channel Nos.30 and 35, we have to take into account the variation of the cloud geometrical characteristics because of the thermal emission contribution. Hence, we considered inhomogeneous clouds with a con-

stant geometrical depth of 0.3 km, but 3 different cloud base heights of 0.5, 0.8, and 1.10 km respectively. Each cloud cell is assumed presently to have vertically uniform microphysical and optical properties. We will evaluate biases of retrieved cloud parameters due to this constant cloud depth assumption in section 5.

[23] Radiance fields were computed for five wavelengths 0.544, 1.6, 2.15, 3.65 and 10.80 μm, which correspond to the maximal response of GLI spectral channel Nos. 8, 28, 29, 30, and 35 respectively. For 0.544, 1.6, and 2.15 μm, radiance simulations were done for surface albedo values of 0, 0.10, and 0.20, while the surface albedo was fixed to 0.05 and 0.0 respectively for 3.65 and 10.80 μm. The limited range of albedo is assumed because our primary objective is the application of the method to the clouds over ocean. For the reason of simplicity, the underlying surface is assumed as Lambertian, even if this assumption is questionable. The radiance fields at 3.65 and 10.80 μm have important contribution from cloud layer and earth surface thermal emission; we computed them for 5 surface temperatures of respectively 283, 288, 293, 303 and 313 K. As for the temperature profile, the US standard temperature profile was shifted globally as a function of surface temperature. Radiance fields were computed for the following solar incidence-viewing configuration:

[24] - 10 solar incidence angles (from 0° to 67.5 by step of 7.5°) except thermal infrared bands (channel No.35).

[25] - 130 viewing directions (from 0° to 67.5° by step of 7.5° for zenithal angle and from 0° to 180° by step of 15° for azimuthal angle).

[26] Our radiance database for inhomogeneous and fractional clouds contains presently about 600 simulations of 6.4 km × 6.4 km cloud domain, which represents roughly a year of continuous running of COMPAQ ES40 Workstation (4 processors and 8 Gbytes of RAMs). This very time-consuming database preparation is the main drawback of the MNN approach, which explains why our radiance database is limited presently to only 4 cloud scenes of constant cloud depth and why we could include neither oxygen absorption band nor non-flat-top inhomogeneous clouds in the present radiance database.

### 3.4. Characteristics of Cloud Properties and Radiance Data at Observation Pixel Scale

[27] Before discussing MNN training, we have to investigate what kinds of correlations exist between cloud parameters and corresponding radiance data. We computed radiance data at (1 km × 1 km) pixel for 5 wavelengths 0.544, 1.6, 2.15, 3.65 and 10.80 μm and 3 standard deviations of radiance estimated over (1 km × 1 km) pixel from 0.25 km × 0.25 km pixel at 0.544, 1.60, and 2.15 μm. We will briefly discuss below only the correlation between the cloud parameters and radiance data from all the correlation analyses done with these data. Table 2 shows the correlation coefficients between the cloud parameters and radiance data; we also presented coefficients of multiple determination $(\Gamma_{multi})^2$, which measure the fraction of variance of a dependent variable which can be explained by a linear combination of explanatory variables [*Legendre and Legendre*, 1998].

[28] First of all, the coefficients of multiple determination indicate that the variances of cloud parameters ($\bar{\tau}_p$, $\bar{r}_p$, $\sigma_{\tau.p}$,

**Table 2.** Correlation Coefficients Between Cloud Parameters and Radiance Data: Coefficients of Multiple Determination $[(\Gamma_{multi})^2]$ and Correlation Coefficients[a]

| | $(\Gamma_{multi})^2$ | $R_{0.544}$ | $R_{1.60}$ | $R_{2.15}$ | $R_{3.65}$ | $R_{10.80}$ | $\sigma_{R0.544}$ | $\sigma_{R1.60}$ | $\sigma_{2.15}$ |
|---|---|---|---|---|---|---|---|---|---|
| $\bar{\tau}_p$ | 0.984 | 0.952 | 0.818 | 0.684 | 0.184 | −0.622 | 0.344 | 0.008 | −0.079 |
| $\bar{r}_p$ | 0.836 | 0.673 (0.237) | 0.590 (−0.110) | 0.450 (−0.454) | −0.033 (−0.878) | −0.724 (−0.163) | 0.041 (−0.120) | −0.285 (−0.426) | 0.382 (−0.497) |
| $\sigma_{\tau.p}$ | 0.936 | 0.665 | 0.487 | 0.365 | −0.079 | −0.274 | 0.747 | 0.444 | 0.299 |
| $\sigma_{r.p}$ | 0.559 | 0.184 | 0.079 | −0.032 | −0.329 | −0.237 | 0.332 | 0.085 | −0.039 |
| $\bar{f}_p$ | 0.875 | 0.740 | 0.842 | 0.828 | 0.595 | −0.835 | 0.001 | −0.209 | −0.240 |
| $\bar{T}_p$ | 0.651 | 0,003 | 0,001 | 0,001 | 0,002 | 0,462 | 0.016 | 0.004 | 0,000 |

[a]Numbers in parentheses correspond to almost totally cloudy pixels ($\bar{f}_p > 0.9$). $\bar{\tau}_p$, mean optical thickness; $\bar{r}_p$, mean effective radius; $\sigma_{\tau.p}$, standard deviation of optical thickness; $\sigma_{r.p}$, standard deviation of effective radius; $\bar{f}_p$, fractional cloud cover; $\bar{T}_p$, cloud top temperature. $R_{0.544}$, $R_{1.60}$, $R_{2.15}$, $R_{3.65}$, $R_{10.80}$: radiances of 0.544, 1.6, 2.15, 3.65 and 10.80 μm. $\sigma_{R0.544}$, $\sigma_{R1.60}$, $\sigma_{R2.15}$, standard deviations of radiance of 0.544, 1.6, and 2.15 μm computed from $0.25 \times 0.25$ km$^2$ pixels.

$\sigma_{r.p}$, $\bar{f}_p$ and $\bar{T}_p$) can be explained up to about 98%, 84%, 94%, 56%, 88% and 65% respectively by linear combinations of 8 radiance data ($R_{0.544}$, $R_{1.60}$, $R_{2.15}$, $R_{3.65}$, $R_{10.80}$, $\sigma_{R0.544}$, $\sigma_{R1.60}$, $\sigma_{R2.15}$). This implies that $\bar{\tau}_p$ and $\sigma_{\tau.p}$ might be retrieved 'almost' by using simple linear multivariate regression, while the other cloud parameters, in particular $\sigma_{r.p}$, require probably more complex non-linear regression. This finding justifies the present retrieval of cloud parameters based on the application of MNNs, and not on linear multivariate regressions.

[29] Table 2 suggests that the information about the cloud parameters $\bar{\tau}_p$, $\bar{r}_p$, and $\bar{f}_p$ is essentially carried by $R_{0.544}$, $R_{1.60}$, $R_{2.15}$, $R_{3.65}$, and $R_{10.8}$, while the information about the cloud parameters $\sigma_{\tau.p}$ and $\sigma_{r.p}$ is more widespread. However, these correlation coefficients do not provide a clear-cut interpretation about the dependency of cloud parameters on these radiance data, because of the redundancy between these explanatory variables. The correlation coefficients of $\bar{\tau}_p$ indicate that its retrieval depends on $R_{0.544}$, $R_{1.60}$, $R_{2.15}$ and $R_{3.65}$ in decreasing order, which corresponds to a decreasing sensitivity of these radiances on the optical thickness. The correlation is also important with $R_{10.80}$, which is because the optical thickness is associated with fractional cloud cover, and thermal radiation emitted by the ground is more or less transmitted as a function of fractional cloud cover. The correlation coefficients of $\bar{r}_p$ show curiously that its retrieval does not depend on $R_{2.15}$ or $R_{3.65}$, but on $R_{0.544}$ and $R_{1.60}$. This can be explained by the fact that the effect of optical thickness should be first removed from $R_{1.60}$, $R_{2.15}$ and $R_{3.65}$ for fractional cloud condition. The dependency on $R_{2.15}$ and $R_{3.65}$ is recovered when we looked at totally cloudy pixels (number in parenthesis); in this case, the correlation coefficients of $\bar{r}_p$ show that its retrieval depends on a combined contribution of $R_{1.60}$, $R_{2.15}$, and $R_{3.65}$ all of which are informative on the effective radius to some degree. The behavior of correlation coefficients of $\sigma_{\tau.p}$ is quite similar to those of $\bar{\tau}_p$ with a notable difference that it has a rather high correlation with $\sigma_{R0.544}$, which implies that $\sigma_{R0.544}$ carries independent information about the sub-pixel inhomogeneity of optical thickness. We do not find such results with the correlation coefficients between $\sigma_{r.p}$ and $\sigma_{R1.60}$, $\sigma_{R2.15}$, but it should be reminded that $\sigma_{r.p}$ is the least explained of the 5 cloud parameters by linear multivariate regression of radiance data as suggested by its moderate coefficient of multiple determinations. Naturally, the correlations coefficients of $\bar{f}_p$ and $\bar{T}_p$ indicate that their retrieval depends mainly on $R_{10.80}$. The correlation coefficients of $\bar{f}_p$ with other mean radiances

are quite high because the present database is composed only of cloud domain with fractional cloud cover and no overcast cloud domain.

## 4. Retrieval Procedure of Cloud Parameters of Inhomogeneous and Fractional Clouds

### 4.1. General Structure of Retrieval Procedure

[30] The procedure of cloud parameter retrieval developed in the present study comprises two distinct steps (Figure 2). The first step is the interpolation-correction of radiance data. The channels Nos. 8, 28, and 29 require the interpolation to the nearest MNN I-V configuration and the correction of albedo effect for both the area-averaged radiance and standard deviation. The channel No.30 requires the interpolation to the nearest MNN I-V configuration and the correction of emission effects, and the channel No.35 only the interpolation to the nearest MNN I-V configuration. The interpolation and correction have been done in one step instead of doing them in two separate steps. The second step is the cloud parameter retrieval as such from the interpolated and corrected radiance data. FIG01 investigated only the feasibility of this second step
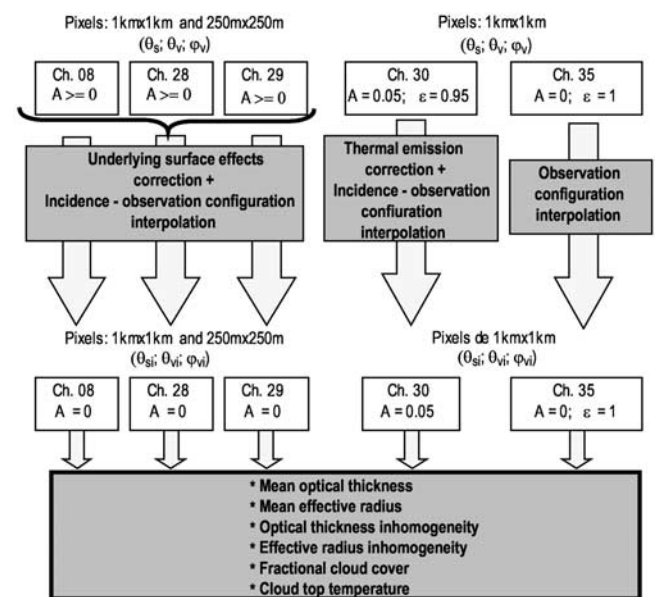


**Figure 2.** General organization of cloud parameter retrieval procedure.
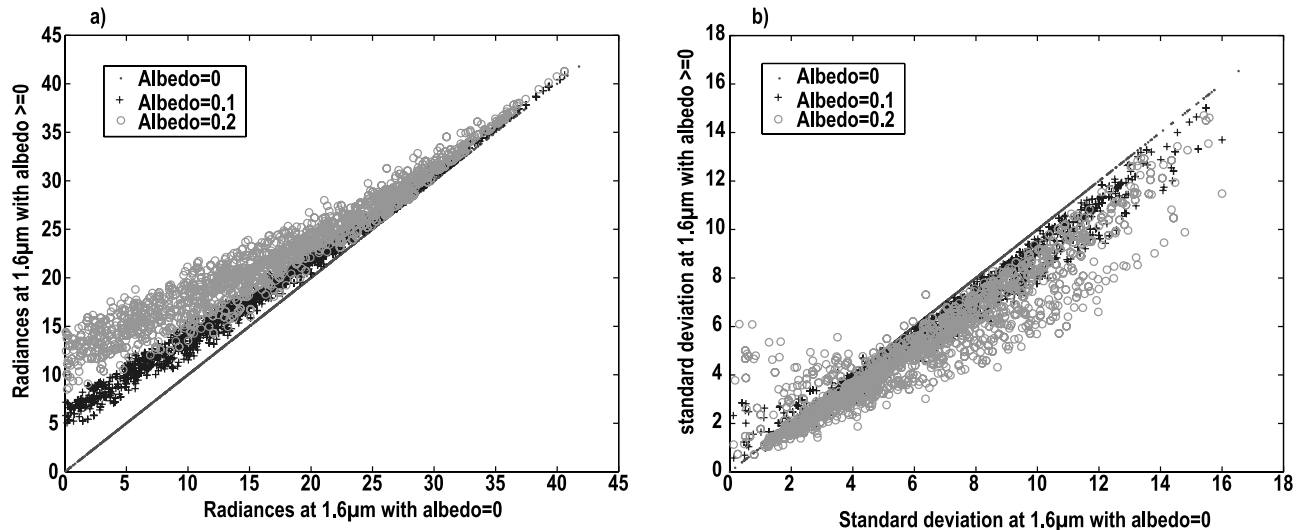
**Figure 3.** (a) Area-averaged radiances at 1.6 μm with underlying reflecting surface (albedo: 0, 0.1 and 0.2) as a function of radiances at 1.6 μm above totally absorbing surface. (b) Standard deviation of radiance at 1.6 μm with underlying surface (albedo: 0, 0.1 and 0.2) as a function of standard deviation of radiances at 1.6 μm above totally absorbing surface, ($\theta_0 = 30°$, $\varphi_v = 90°$, $\theta_v = 30°$).

without discussing the feasibility of the first step that is essential for the development of the cloud parameter retrieval of inhomogeneous clouds. The main reason to separate the cloud parameter retrieval into two steps is that no earlier study has showed that we could do such interpolation-correction for inhomogeneous clouds with acceptable accuracy.

### 4.2. Interpolation-Correction MNNs

[31] To interpolate radiance from a given I-V configuration to the nearest MNN I-V configuration, we have to include all the angular deviations between these two configurations as input vector components. Hence, to train the interpolation-correction MNN for a given MNN I-V configuration with solar incidence angle $\theta_0(i)$, viewing azimuth angle $\varphi_v(j)$, and viewing zenithal angle $\theta_v(k)$, we have to consider a total of 27 I-V configurations, which includes 26 neighbor I-V configurations with $[\theta_0(i \pm 1)$, $\varphi_v(j \pm 1)$, $\theta_v(k \pm 1)]$ and target configuration $[\theta_0(i)$, $\varphi_v(j)$, $\theta_v(k)]$ itself in the training data set. The interpolation can be easily done in theory if the knowledge of the optical thickness and effective radius is available. Instead, we have to replace here this knowledge by the knowledge of radiances informative on these parameters. We also have to include some ancillary data to do this interpolation-correction: the ground surface albedo if radiance depends on the surface albedo and the ground surface temperature if radiance depends on the surface temperature. Since the ground surface albedo depends on surface types and varies nonlinearly with the wavelength [*Lucht et al.*, 2000], we have to include as many surface albedos as the number of wavelengths as input vector components.

### 4.2.1. Interpolation and Correction of Albedo Effect for 0.544, 1.6 and 2.15 μm Channels

[32] Figures 3a and 3b show the effect of albedo on the area-averaged radiance and standard deviation of radiance for a wavelength of 1.6 μm; the solar incidence angle is 30°, viewing direction ($\theta_v = 30°$, $\varphi_v = 90°$) and the ground

surface albedo of 0, 0.1 and 0.2 respectively. The general features observed in Figures 3a and 3b are roughly the same when the solar incidence angle and viewing direction change, but also when the wavelength changes from 1.60 μm to 0.544 and 2.15 μm. The albedo effect is not uniform and varies with the optical thickness, fractional cloud cover and inhomogeneity parameter. As expected, the albedo effect in the area-averaged radiance, which is always positive, is small for large optical thickness while it becomes large and more dispersed for small optical thickness. The albedo effect in the standard deviation of radiance, which is negative in most of cases, is large and dispersed for large optical thickness, while it becomes generally small and less dispersed for small optical thickness. There are some cases with large positive effect for small optical thickness, which correspond to pixels with small fractional cover over underlying surface with albedo of 0.2. This particular behavior of albedo effect on the standard deviation can be easily explained by the fact that the standard deviation of radiance increases because some radiance comes from clear sky region when earth surface is reflecting, while no radiance comes from clear sky region when earth surface is totally absorbing.

[33] The output and input vectors to the interpolation-correction MNNs are:

[34] Output vector with 2 components:

[35] - Area-averaged radiance and standard deviation of radiance at one of the three wavelengths (0.544, 1.6, 2.15 μm) over totally absorbing earth surface in the nearest MNN I-V configuration;
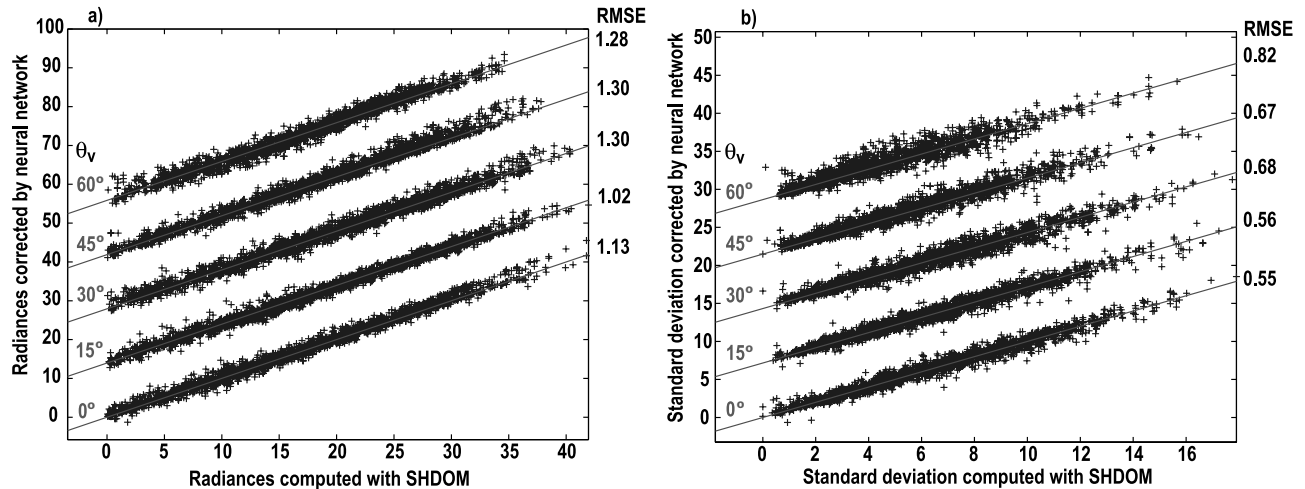
[36] Input vector with 12 components:

[37] - 3 angular distances between an arbitrary I-V configuration to the nearest MNN I-V configuration;

[38] - 3 area-averaged radiances ($R_{0.544}$, $R_{1.60}$, $R_{2.15}$) measured at an arbitrary I-V configuration;

[39] - 3 standard deviations of radiance ($\sigma_{R0.544}$, $\sigma_{R1.60}$, $\sigma_{R2.15}$) estimated from 250 m × 250 m pixels;

[40] - 3 values of albedo of 0.544, 1.60 and 2.15 μm.

**Figure 4.** (a) Interpolated-corrected area-averaged radiance at 1.6 μm as a function of target area-averaged radiance at 1.6 μm. (b) Interpolated-corrected standard deviation of radiance at 1.6 μm as a function of target standard deviation of radiances at 1.6 μm. For each viewing angle presented, the values are shifted upward for better visual clarity, ($\theta_0 = 30°$, $\varphi_v = 90°$).

[41] The training was done with 10000 randomly selected patterns, and the generalization performance was estimated with other 5000 randomly selected patterns; in principle there is only a few overlapping patterns in the training and generalization data sets. There are 1170 MNNs to train, each corresponding to a MNN I-V configuration (9 solar incidence angles × 130 observation directions).

[42] Interpolated-corrected radiance is shown in Figure 4a and standard deviation in Figure 4b as a function of target values for 5 viewing zenithal angles ($\theta_v = 0°$, 15°, 30°, 45°, 60°) and a viewing azimuth angle of 90°. The input vectors used for this test are 'error-free' in the sense that radiance values computed by SHDOM are directly used without any additional errors. The RMSE of interpolated-corrected area-averaged radiance varies with MNN I-V configurations, but remains less than 2 $W.m^{-2}.sr^{-1}$ for most of the MNN I-V configurations; a maximum RMSE of 3 $W.m^{-2}.sr^{-1}$ occurs in the backward scattering direction. Since the dispersion of interpolated-corrected radiance changes slightly with its 'target' values, the relative error would remain less than 5% for large target values, while it becomes more than 10% for small target values.

[43] The general features of interpolated-corrected standard deviation do not differ very much from those observed for the area-averaged radiance, except that the corresponding RMSE remains lower than 1 $W.m^{-2}.sr^{-1}$ for most of the MNN I-V configurations. The dispersion increases with the increase of viewing zenithal angle. This behavior can be explained by the fact that the more oblique the viewing direction is, the more uniform the cloud scene appears; this can be seen by the more limited range of standard deviation for the viewing zenithal angle of 60° and the ones for 30° and 0°. The relative error in interpolated-corrected standard deviation is slightly larger than that obtained for the area-averaged radiance. These features of interpolation-correction MNNs vary slightly for the other wavelengths (0.544 μm and 2.15 μm).

### 4.2.2. Interpolation and Correction of Emission Effect for 3.65 and 10.80 μm Channels

[44] Since information on the effective radius is mostly carried by reflected solar radiation, we have to remove the contribution of thermal emission from measured 3.65 μm radiance. This correction is an important source of uncertainty in the retrieved cloud effective radius. *Nakajima and Nakajima* [1995] gave a brief summary of different earlier methods. *Coakley and Davies* [1986] used an empirical relation between night 3.65 μm radiances and thermal infrared radiances to remove the contribution of emission at 3.65 μm. *Kaufman and Nakajima* [1993] subtracted thermal radiation from 3.65 μm radiance by using an effective temperature estimated from thermal infrared radiance and an optical thickness guessed from visible channel. Recently, *Kawamoto et al.* [2001] have proposed a more sophisticated method in which they integrated tropospheric temperature and humidity profiles provided by a meteorological analysis as ancillary data. Our method does not take presently into account of water vapor amount in the atmosphere, but it can easily be modified to include them. The thermal emission radiation is to be removed simultaneously with the interpolation of 3.65 μm radiance component due to reflected solar radiation to the nearest MNN I-V configuration. As for the thermal infrared radiance, we have to interpolate it to the nearest MNN I-V configuration if we want to include radiance at a thermal infrared wavelength (10.80 μm in our case) as an input vector component for cloud parameter retrieval. As seen in Table 2, the thermal infrared radiance is an important radiance data to retrieve the fractional cloud cover, in addition to its evident importance for the retrieval of cloud top temperature.

[45] Figure 5 represents the thermal emission at 3.65 μm from inhomogeneous cloud pixels as a function of corresponding radiance at 10.80 μm for an observation direction of ($\theta_0 = 30°$, $\varphi_v = 90°$). The thermal emission at 3.65 μm exhibits some significant dispersion due to optical thickness, effective radius, and fractional cloud cover in addition to its dependency on surface temperature and cloud
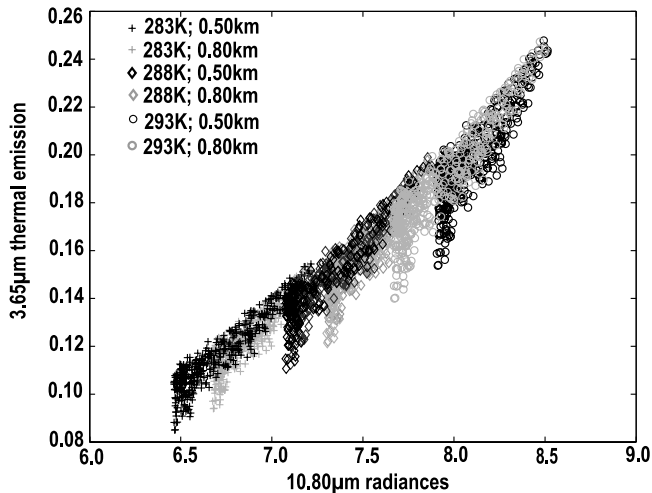
**Figure 5.** The 3.65 μm thermal emission as a function of 10.80 μm radiances of inhomogeneous clouds with variable optical thickness, effective radius, cloud base height, and underlying surface temperature, ($\varphi_v = 90°$, $\theta_v = 30°$).

top altitudes. To approximate these points with a unique empirical relation as proposed by *Coakley and Davies* [1986] results necessarily in a rather important error in $R_{3.65}$ and consequently in retrieved effective radius.

[46] The output and input vectors to the interpolation-thermal emission correction MNNs are

[47] Output vector:

[48] - area-averaged radiance due to the thermal emission at 3.65 μm at the nearest MNN configuration;

[49] Input vector with 10 components:

[50] - 3 angular distances between an arbitrary I-V configuration to the nearest MNN I-V configuration;

[51] - 4 area-averaged radiances ($R_{0.544}$, $R_{2.15}$, $R_{3.65}$, $R_{10.80}$) measured at an arbitrary I-V configuration;

[52] - 2 values of albedo for two wavelengths (0.544 and 2.15 μm);

[53] - 1 surface temperature.

[54] For the interpolation of thermal radiance at 10.80 μm, we used the same MNN architecture as the one for the 3.65 μm interpolation-correction. In this case, the output vector is the area-averaged radiance due to thermal emission at 10.80 μm at the nearest MNN configuration, while the input vector is the same, but without $R_{3.65}$.

[55] The training of MNNs was done with 5000 patterns randomly chosen from the database. The training was done for each MNN I-V configuration in spite of the fact that thermal emission fields are axisymmetrical with respect to the vertical direction. This is because 0.544 μm and 2.15 μm radiances used as input vector components depend on the solar incidence and viewing directions. Figure 6 presents the 3.65 μm radiance corrected for its thermal emission as a function of target values for 5 viewing zenithal angles ($\theta_v = 0°$, 15°, 30°, 45°, 60°) and a viewing azimuth angle of 90°; the solar incidence angle is 30°. The input vectors used for this test are also 'error-free'. There is no significant variation of dispersion with the viewing zenithal angle. The polar representation of RMSEs (not shown here) show that the RMSE remains less than 0.017 W.m$^{-2}$.sr$^{-1}$ for most of the MNN I-V config-

urations; a maximum RMSE of about 0.025 W.m$^{-2}$.sr$^{-1}$ occurs in the backward scattering direction.

[56] Figure 7 shows the generalization performance of interpolation MNNs for thermal infrared wavelength 10.80 μm for the same MNN I-V configurations. This figure shows no significant variation of dispersion with the viewing zenithal angle up to 45°.

### 4.3. Cloud Parameter Retrieval MNNs

[57] Radiance data corrected for the albedo effect and/or thermal emission effect were used to train cloud parameter retrieval MNNs. The input vector components may vary from one cloud parameter to the others because of redundant information content. However, in this study, we have used all the available radiance data for every cloud parameter without any particular effort to choose a minimal number of informative data for each cloud parameter. The architecture of MNNs is the same as those used for the interpolation-correction. We performed two series of training:

[58] - the 1st series of training was done with input vectors composed of 5 area-averaged radiances (0.544, 1.6, 2.15, 3.65 and 10.80 μm) and surface temperature as ancillary data;

[59] - the 2nd series of training was done with input vectors composed of 5 area-averaged radiances (0.544, 1.6, 2.15, 3.65 and 10.80 μm) and surface temperature as ancillary data and 3 standard deviations of radiance (0.544, 1.6 and 2.15 μm).

[60] The two training sets are composed of the same 2000 observation pixels we have randomly selected from our database so that the performance of MNNs might be easily compared between the two series.

[61] For the 1st series of training, we are trying to retrieve 6 cloud parameters from 5 radiance data; the 6th input vector component, surface temperature, is ancillary and does not depend on any cloud property. From this point of view, the 1st series of training might be flawed in its
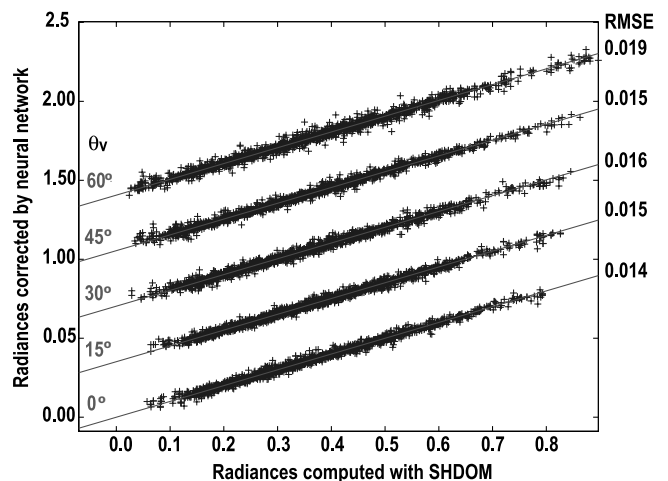


**Figure 6.** Reflected solar radiation component of 3.65 μm radiance computed with MNN as a function of its true values computed with SHDOM. For each viewing angle presented, the values are shifted upward for better visual clarity, ($\theta_0 = 30°$, $\varphi_v = 90°$).
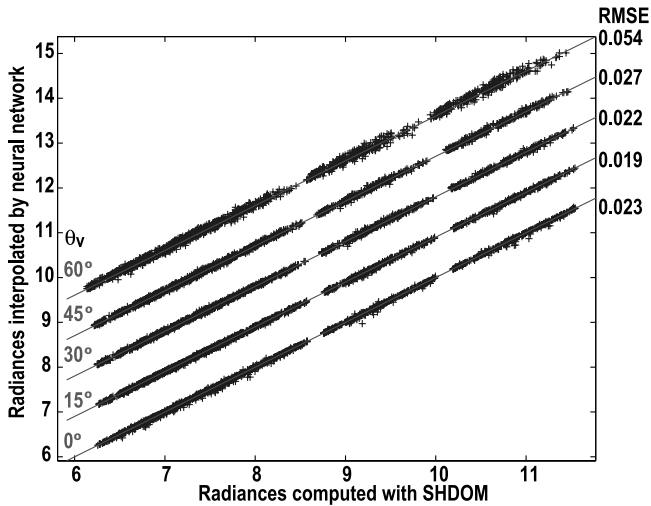
**Figure 7.** The 10.80 μm radiance interpolated to the nearest MNN I-V configuration as a function of the corresponding true values computed with SHDOM. For each viewing angle presented, the values are shifted upward for better visual clarity, ($\theta_0 = 30°$, $\varphi_v = 90°$).

principle, and it might impose spurious correlation between retrieved cloud parameters. Furthermore, since multispectral radiance data are highly correlated data, we have to extract independent and informative part from measured radiance, which varies with cloud characteristics and I-V configuration and may become too small to be extracted for certain cloud conditions and/or viewing configuration.

[62] Figures 8a–8f present the performance of two types of cloud parameter retrieval MNNs for a solar incidence angle of 30°. RMSEs are plotted as a function of viewing zenithal angle for 3 conditions: training, generalization with error-free input vectors, and generalization with input vectors with uniform random error less than 2%. The RMSEs obtained for error-free input vectors represent a reference intrinsic dispersion of cloud parameter retrieval MNNs. These figures show clearly that the additional input vector components $\sigma_{R0.544}$, $\sigma_{R1.60}$, and $\sigma_{R2.15}$ can improve significantly the training and generalization performance of cloud parameter retrieval MNNs. However, as suggested by *Szczap et al.* [2000a, 2000b] and FIG01, the area-averaged radiance itself carries the information about the sub-pixel cloud inhomogeneity, because the sub-pixel cloud inhomogeneity in optical thickness and effective radius can be
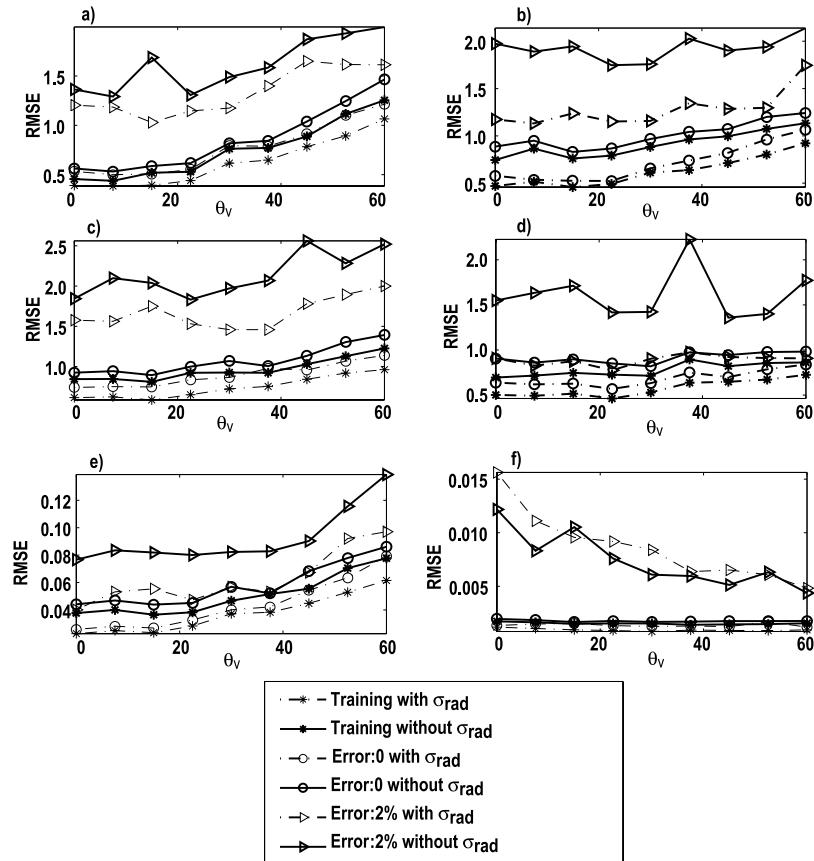


**Figure 8.** Comparison of the performance of two types of cloud parameter retrieval MNNs. ($\theta_0 = 30°$, $\varphi_v = 90°$). The first one trained with additional input components $\sigma_{R0.544}$, $\sigma_{R1.60}$, and $\sigma_{R2.15}$, and the second one without additional input components $\sigma_{R0.544}$, $\sigma_{R1.60}$, and $\sigma_{R2.15}$. (a) Mean optical thickness, (b) mean effective radius, (c) optical thickness inhomogeneity, (d) effective radius inhomogeneity, (e) fractional cloud cover, and (f) cloud top temperature.
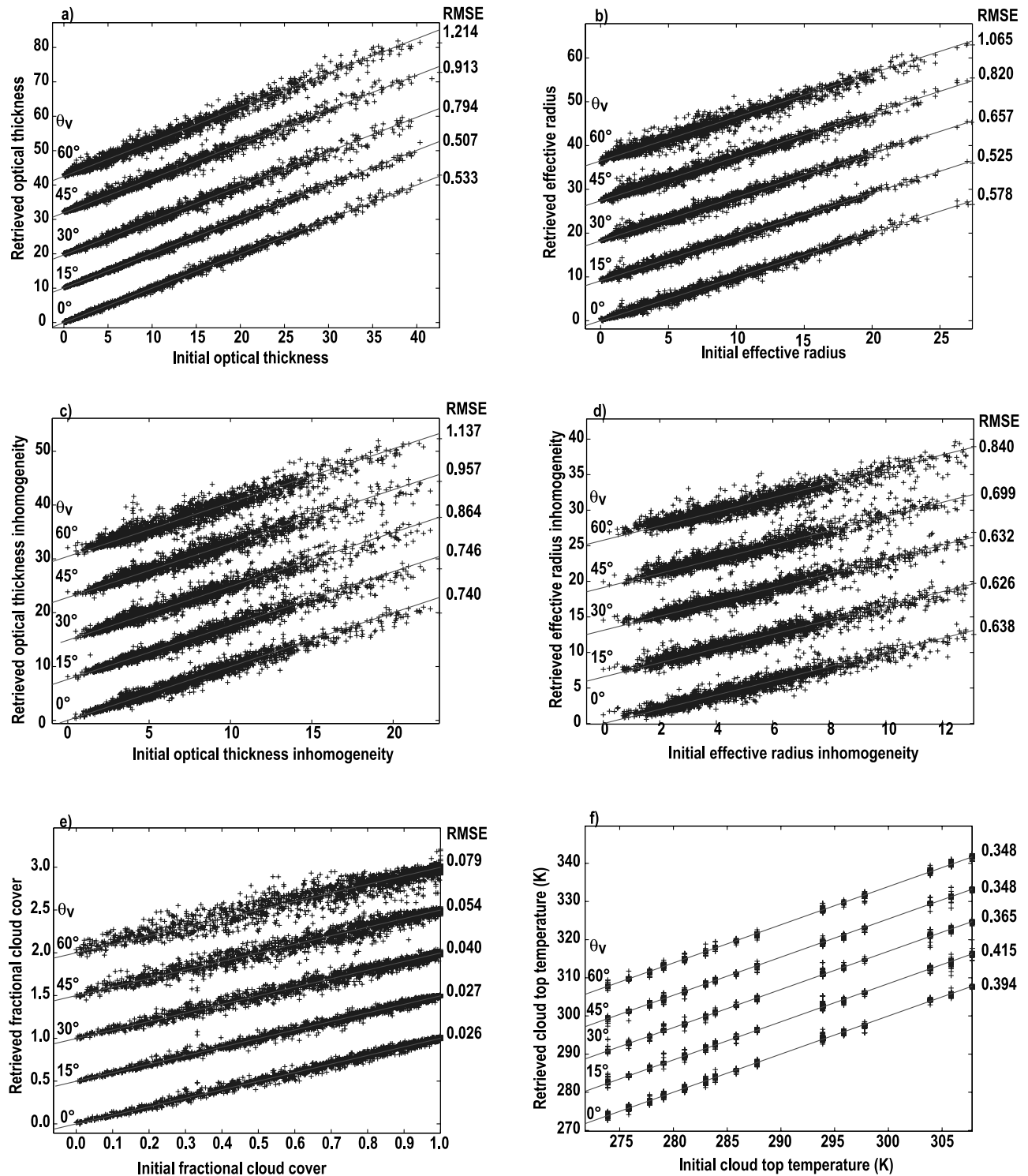
**Figure 9.** Comparison between retrieved and initial cloud parameters for 5 observation directions. ($\theta_0$ = 30°, $\varphi_v$ = 90°). (a) Mean optical thickness, (b) mean effective radius, (c) optical thickness inhomogeneity, (d) effective radius inhomogeneity, (e) fractional cloud cover, and (f) cloud top temperature. For each viewing angle presented, the values are shifted upward for better visual clarity.

retrieved without the additional input components of $\sigma_{R0.544}$, $\sigma_{R1.60}$, and $\sigma_{R2.15}$.

[63] The retrieval of the mean optical thickness $\bar{\tau}_p$ is improved by the inclusion of standard deviations of radiance in spite of what the linear multiple correlation analysis

has suggested above (cf. Table 2). However, the improvement may appear less significant for large zenithal angles $\theta_v > 30°$ than for small zenithal angles $\theta_v < 30°$, which can be explained by the fact that $\sigma_{R0.544}$, $\sigma_{R1.60}$, and $\sigma_{R2.15}$ carry less information about the sub-pixel cloud inhomogeneity

for large viewing zenithal angles than for small viewing zenithal angles as discussed in 4.2. Compared with the limited improvement for $\bar{\tau}_p$ and $T_{top}$, the retrieval of other cloud parameters ($\bar{r}_p$, $\sigma_{\tau.p}$, $\sigma_{r.p}$, and $\bar{f}_p$) is significantly improved for all observation directions. Consequently, we will include the standard deviations of radiance $\sigma_{R0.544}$, $\sigma_{R1.60}$, and $\sigma_{R2.15}$ as input vector components in the present retrieval procedure.

[64] In Figure 9, we plotted cloud parameters retrieved with additional input components $\sigma_{R0.544}$, $\sigma_{R1.60}$, and $\sigma_{R2.15}$; the solar incidence angle is 30° and the viewing direction ($\theta_0 = 30°$, $\varphi_v = 90°$). The overall performance of the cloud parameter retrieval MNNs is relatively satisfactory in spite of an inherent dispersion. The dispersion tends to increase with the viewing zenithal angle for cloud parameters $\bar{\tau}_p$, $\bar{r}_p$, $\sigma_{\tau.p}$, $\sigma_{r.p}$ and $\bar{f}_p$. These dispersions may be due to three factors. Firstly, the MNN is only a method to approximate a multivariate function without knowing exactly its functional form, which necessarily implies some degree of intrinsic approximation errors. Secondly, the correspondence between available radiance data and cloud parameters is not a strict one-to-one correspondence, but an approximate one with inherent dispersions. The third factor is that a pixel size of 1 km is probably too small to neglect the contributions of neighboring pixels even for a geometrical cloud depth of 0.3 km [Szczap et al., 2000a].

[65] In order to compare the cloud parameter retrieval under the inhomogeneous cloud assumption with the one under the plane parallel homogeneous cloud assumption, we trained specially an MNN with 2 input vector components ($R_{0.544}$ and $R_{3.65}$) and 2 outputs (optical thickness and effective radius) under the plan-parallel homogeneous cloud assumption. The radiance data used for this test come from bounded cascade clouds; the solar incidence angle is 30° and the viewing direction is $\varphi_v = 60°$ and $\theta_v = 15°$. We plotted the cloud parameters retrieved under the homogeneous cloud assumption in addition to the ones retrieved under the inhomogeneous cloud assumption (Figure 10). We separated them into two groups: the first group contains the retrieved parameters for $\bar{f}_p < 0.9$) and the second group for $\bar{f}_p \geq 0.9$.

[66] The plane-parallel homogeneous optical thickness shows an approximately linear variation with the target optical thickness, except that it underestimates significantly the target optical thickness. This behavior can be easily explained by the fact that $R_{0.544}$ varies mostly with the optical thickness; for a given mean optical thickness it is always smaller for inhomogeneous clouds than for homogeneous ones. The retrieved optical thicknesses of the first group tend to be slightly larger than those of the second group, because a larger fractional cloud cover exhibits usually a larger sub-pixel inhomogeneity. A small dispersion of retrieved optical thickness for small to moderate optical thickness can be explained by the fact that the radiance increases very rapidly for small to moderate optical thickness, and as a consequence, the retrieved optical thickness exhibits fairly small dispersions in spite of the effect of cloud inhomogeneity. The lack of large dispersion for moderate to large true mean optical thickness may be due to the fact that there are only a few observation pixels with large optical thickness in our radiance database.

[67] As for the effective radius, the situation differs considerably from the one for the optical thickness. The homogeneous effective radius increases roughly with the true mean effective radius with a very large dispersion for $\bar{r}_p > 10$ μm, while it also exhibits a clear bias in addition to the large dispersion for $\bar{r}_p \leq 10$ μm. The plane-parallel effective radius tends to overestimate the true mean effective radius. This fact agrees with earlier finding that the 'effective' single scattering albedo becomes smaller than the true single scattering albedo when an inhomogeneous cloud is treated as a plane-parallel homogeneous cloud [Szczap et al., 2000a]. The effective radius of the first group exhibits much larger dispersion than that of the second group, which shows that the large dispersion of retrieved effective radius is due mostly to the effect of fractional cloud cover within observation pixels. The very large dispersion, especially large biases observed for $\bar{r}_p \leq 10$ μm, may be due to the occurrence of multiple solutions that results in a poorer performance of the MNNs in that range of effective radius.

## 5. Performance of the Whole Retrieval Procedure

[68] Since we have ascertained the feasibility of each step in the MNN retrieval procedure, we have to test the whole retrieval procedure (the interpolation-correction step and cloud parameter retrieval step).

### 5.1. Clouds Generated With Bounded Cascade Cloud Model

[69] Since all the MNNs have been trained with radiance data computed for inhomogeneous clouds with a cloud depth of 0.3 km, we need to evaluate biases in retrieved cloud parameters when we apply these MNNs to inhomogeneous clouds with different geometrical cloud characteristics. Hence, we applied the retrieval procedure to following two bounded cascade clouds:

[70] 1 – A bounded cascade cloud with $\tilde{\tau}_D = 12$, $\tilde{r}_D = 10$ μm, and $\tilde{f}_D = 0.7$ with a geometrical cloud depth of 0.30 km; the radiance fields are computed for solar incident angle of 27° and underlying surface albedo of 0.12, 0.15, 0.05, 0.05 and 0 respectively for 0.544, 1.6, 2.15, 3.65 and 10.80 μm with viewing angular resolutions of ($\delta\theta = 3.75°$, $\delta\varphi = 7.5°$).

[71] 2 – A bounded cascade cloud with $\tilde{\tau}_D = 10$, $\tilde{r}_D = 10$ μm, and $\tilde{f}_D = 0.8$ with a geometrical cloud depth of 0.90 km; the radiance fields are computed for the solar incidence angle of 45° and totally absorbing underlying surface albedo with viewing angular resolutions of ($\delta\theta = 7.5°$, $\delta\varphi = 15°$).

[72] Figures 11a to 11e represent retrieved mean optical thickness, mean effective radius, optical thickness inhomogeneity, effective radius inhomogeneity, and fractional cloud cover; the cloud top temperature has not been retrieved because it is set constant of 283 K. The retrieved parameters are shown for viewing directions of ($\bar{\varphi}_v = 127.5°$, $\bar{\theta}_v = 26.75°$) for 0.3 km cloud and ($\bar{\varphi}_v = 90°$, $\bar{\theta}_v = 30°$) for 0.9 km cloud respectively. These figures show that the cloud parameters of bounded cascade clouds may be retrieved reasonably well in spite of fairly large dispersions inherent to the various underlying assumptions. It is interesting to remark that the geometrical cloud depth does not lead to any visible systematic bias in the retrieved cloud parameters, expect in the fractional cloud cover.
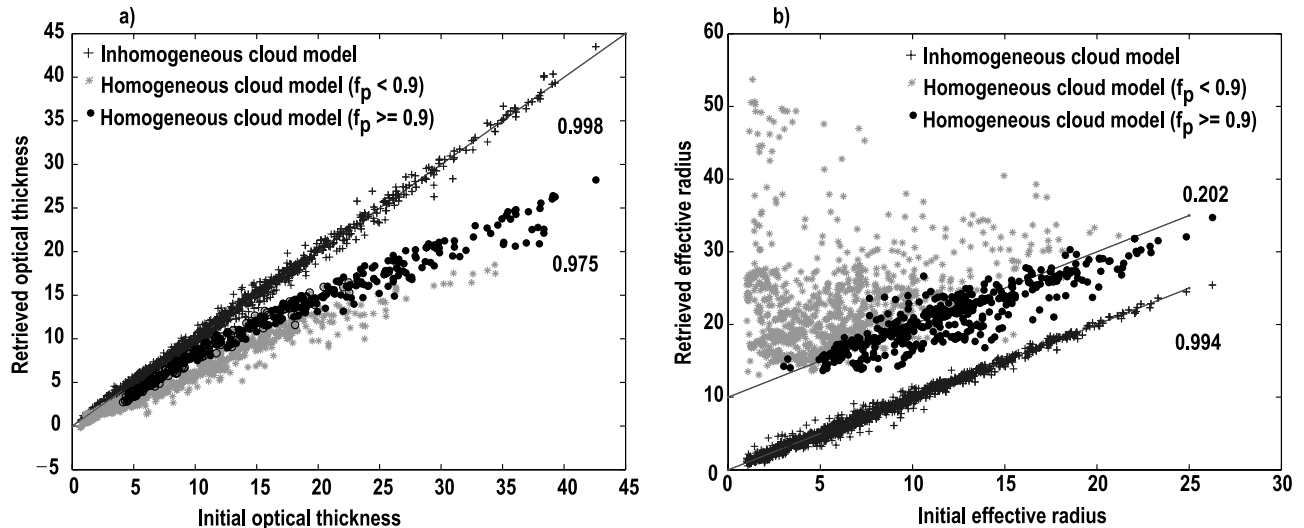
**Figure 10.** Comparisons of optical thickness and effective radius retrieval based on a plan parallel cloud inverse model or on an inhomogeneous cloud model. (a) Optical thickness and (b) effective radius retrieved from a cloud generated with the bounded cascade model. The cloud parameters retrieved under the plane-parallel homogeneous cloud are separated into two groups as a function of fractional cloud cover: $\bar{f}_p < 0.9$ and $\bar{f}_p \geq 0.9$. Solar incidence angle is $30°$. Viewing angles are ($\varphi_v = 60°$, $\theta_v = 15°$).

[73] The optical thickness retrieved for 0.3 km cloud is slightly biased, and its deviation increases with target optical thickness, while optical thickness retrieved for 0.9 km cloud show no systematic bias. In spite of this bias in the optical thickness, the effective radius retrieved for 0.3 km cloud agrees fairly well with the target effective radius with an overall RMSE of 1.90, while the effective radius retrieved for 0.9 km shows an overall RMSE of 1.93. The dispersion is larger for small target effective radius than for large target effective radius. As for the standard deviation of optical thickness of 0.3 km cloud, its RMSE is 2.01, which is much larger than the reference RMSE of cloud parameter retrieval MNN (normally less than 1 as shown in Figure 9c). It also exhibits a slight positive bias for target standard deviations larger than 6, which should be associated with the bias in mean optical thickness. The corresponding RMSE of 0.9 km cloud is 1.14; there seems a slight negative bias for all the range of target standard deviation, which is compatible with the underestimation of $\sigma_{R0.544}$, $\sigma_{R1.60}$, and $\sigma_{R2.15}$ (cf. A.2c). As for the standard deviation of effective radius, retrieved values agree fairly well with the target values for both clouds with RMSEs of 1.13 and 1.12 respectively. The fractional cloud cover retrieved for 0.3 km cloud agrees fairly well with the target values while the one retrieved for 0.9 km cloud exhibits an overestimation for fractional cover less than 0.9. This overestimation should correspond to the underestimation of $\sigma_{R1.60}$ and $\sigma_{R2.15}$ (cf. Figure A2c). This implies that even if fractional cloud cover is associated mainly with $R_{10.80}$ (Table 2), the MNNs still use $\sigma_{R0.544}$, $\sigma_{R1.60}$, and $\sigma_{R2.15}$ as informative input data for the retrieval of fractional cloud cover.

## 5.2. Clouds Generated With Gaussian Process

[74] We have indicated above that the rationale to chose bounded cascade clouds for the preparation of radiance data set is that the exact types of 'direct' inhomogeneous clouds are not important as far as the inhomogeneous clouds are characterized by the first and second order moments of sub-pixel scale variances of cloud parameters. Moreover, all the clouds used for neural network training are flat-top clouds, while it is well known that the cloud top height variation may have important effects on the radiance fields, and consequently on the retrieved optical thickness [Loeb et al., 1998; Varnai, 2000; Iwabuchi and Hayasaka, 2002]. One may ask how the present retrieval procedure performs when it is applied to radiance data of inhomogeneous clouds other than bounded cascade clouds.

[75] We applied the retrieval procedure to two Gaussian inhomogeneous clouds [Barker and Davies, 1992; Loeb et al., 1998] with $\tilde{\tau}_D = 10$, $\tilde{r}_D = 5$ $\mu$m, $\tilde{f}_D = 0.70$: the one with a constant geometrical cloud depth of 0.3 km and the second with non-flat-top cloud. The optical thickness field generated has a spectral slope of $-1.6$ before to add the fractional cloud cover. The non-flat-top cloud was created by using the relation

$$Z_{top} = \langle Z_D \rangle \times \sqrt{\frac{\tau}{\langle \tau_D \rangle}}$$

where $Z_{top}$ represents the geometrical cloud depth of an elementary pixel, and $\langle Z_D \rangle$ the domain mean geometrical cloud depth. The cloud base was set at 0.5 km and the mean geometrical cloud depth at 0.3 km for cloudy part. The radiance fields were computed for a surface albedo of 0.1, 0.1, 0.2, 0.05 and 0 respectively for 0.544, 1.6, 2.15, 3.65 and 10.80 $\mu$m and a solar incident angle of $42°$ with viewing angular resolutions ($\delta\theta = 3.75°$, $\delta\varphi = 7.5°$).

[76] Figures 12a to 12e present the retrieved cloud parameters of these flat-top and non-flat-top clouds for a viewing direction of ($\varphi_v = 127.5°$, $\theta_v = 26.25°$). The ranges of variation of cloud parameters are very much limited for these Gaussian process clouds than the bounded cascade clouds. These figures shows globally
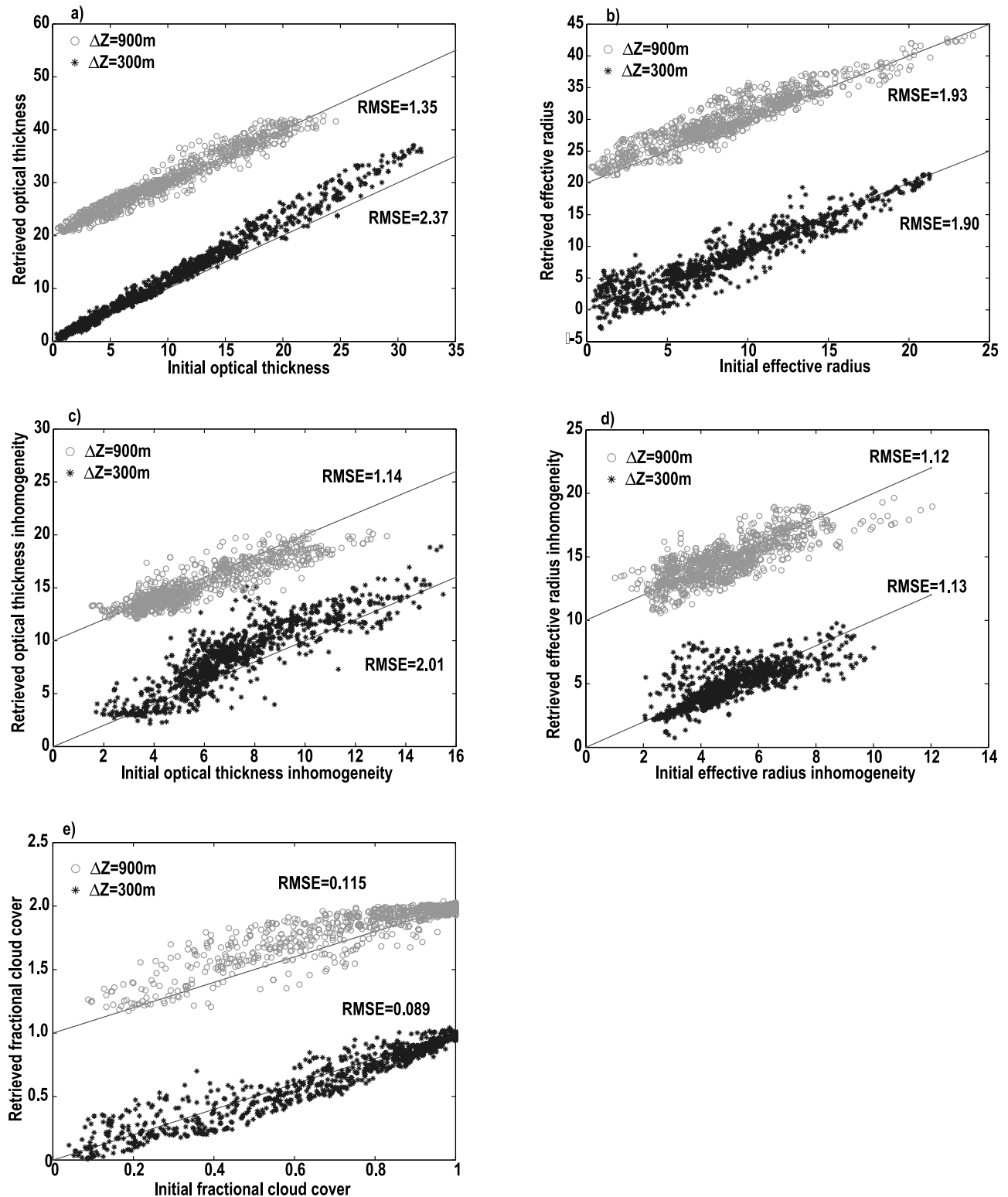
**Figure 11.** Comparison between retrieved and initial cloud parameters for bounded cascade clouds with geometrical cloud depth of 0.3 km and 0.9 km respectively: (a) mean optical thickness, (b) mean effective radius, (c) optical thickness inhomogeneity, (d) effective radius inhomogeneity, (e) fractional cloud cover. Solar incidence angle is 27° for 0.3 km cloud and 45° for 0.9 km (the values are shifted for better visual clarity). Viewing directions are ($\varphi_v = 127.5°$, $\theta_v = 26.75°$) for 0.3 km cloud and ($\varphi_v = 90°$, $\theta_v = 30°$) for 0.9 km.
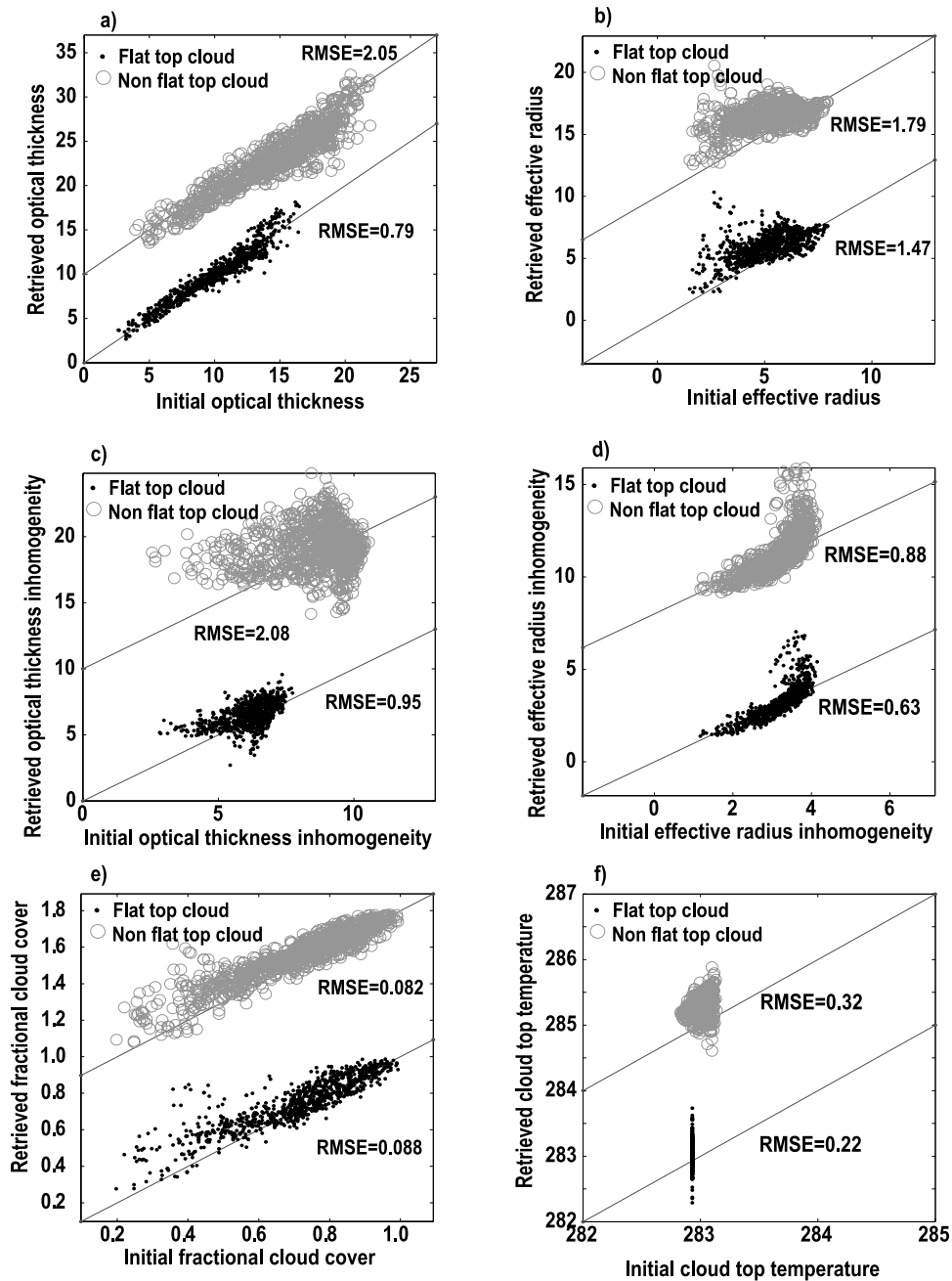
**Figure 12.** Comparison between retrieved and initial cloud parameters for Gaussian process inhomogeneous clouds with flat-top and non-flat-top: (a) mean optical thickness, (b) mean effective radius, (c) optical thickness inhomogeneity, (d) effective radius inhomogeneity, (e) fractional cloud cover and (f) cloud top temperature. Solar incidence angle is $42°$. Observation direction is ($\varphi_v = 127.5°$, $\theta_v = 26.75°$).

that the cloud parameters of Gaussian process clouds can be retrieved with the same order of RMSEs as those of bounded cascade clouds in spite of the MNNs trained with radiance data of the bounded cascade clouds, except some dispersion observed in the optical thickness and its standard deviation of non-flat-top Gaussian process cloud.

[77] The optical thickness retrieved for the flat-top Gaussian cloud agrees well with the target values with any systematic bias such as the one observed for the 0.3 km bounded cascade cloud (Figure 11a). Its standard deviation varies in a very limited range (from 3 to 8) compared with the range from 2 to 16 for the bounded cascade clouds. In spite of an impression of large dispersion (Figure 12c), its RMSE is quite small of only 0.95. However, the retrieved optical thickness and its standard deviation of the non-flat-top cloud exhibit larger dispersion. This increase in the dispersion reflect the fact that the non-flat-top clouds have different radiances and different standard deviation of radiance than the flat-top clouds in visible and slightly absorbing near infrared wavelengths

[*Loeb et al.*, 1998; *Varnai*, 2000; *Iwabuchi and Hayasaka*, 2002]. The figures also show that the dispersions of the other retrieved parameters become larger for the non-flat-top cloud than the flat-top cloud.

[78] The retrieved effective radius of the flat-top cloud agrees fairly well with its target values beyond 5 μm in spite of rather large dispersion, while it overestimates the target values for smaller effective radius; we have not observed such bias for bounded cascade clouds. The corresponding standard deviation also varies in the very limited range (from 2 to 4) compared with the range from 1 to 12 for the bounded cascade clouds. Figure 12d shows the occurrence of overestimation around $\sigma_r = 4$ μm. This may be due to the fact that some input vectors for Gaussian process clouds are not covered by the space defined by the input vectors for bounded cascade clouds. Nevertheless, the RMSEs remain relatively small of only 1.47 for the mean effective radius and 0.63 for its standard deviation. These features are quite similar to those of the non-flat-top cloud. The retrieved effective radius and its standard deviation do not show any systematic bias. The corresponding RMSEs are 1.79 for the mean effective radius and 0.88 for its standard deviation, slightly larger than those observed for the flat-top cloud. This seems to imply that the radiance data that are informative of the effective radius are less affected by the variable cloud top. The fractional cloud cover retrieved for both the Gaussian process cloud agrees reasonably well with the target values for $0.7 < \bar{f}_p$, while it exhibits an overestimation for $\bar{f}_p < 0.7$. This behavior is similar to that observed for the 0.9 km bounded cascade cloud. The retrieval of the mean cloud top temperature also seems to work fairly well for both the Gaussian process clouds.

## 6. Discussions and Perspectives

[79] In the present study, we tested the feasibility of retrieving cloud parameters in case of inhomogeneous and fractional clouds from multispectral and multiscale radiance data, i.e., area-averaged radiance for two different scales of observation pixel, i.e., (1 km × 1 km) pixel and (0.25 km × 0.25 km) pixel respectively. The inverse inhomogeneous cloud with vertically uniform microphysical and optical properties is defined with 6 clouds parameters: mean optical thickness, mean effective radius, fractional cloud cover parameter, inhomogeneity parameter of optical thickness and inhomogeneity parameter of effective radius, and cloud top temperature. The retrieval procedure is based on the application of the mapping neural networks, and it comprises two distinct steps: the interpolation-correction step and the cloud parameter retrieval step.

[80] The interpolation-correction step, though only technical, is one of the key issues for the development of the cloud parameter retrieval. The results showed that the interpolation and correction of radiance data could be done with a good accuracy by using the mapping neural networks. Some biases and dispersions observed in retrieved cloud parameters may suggest that the angular steps $\delta\theta_0 = 7.5°$, $\delta\varphi_v = 15°$, $\delta\theta_v = 7.5°$ we adopted for the radiance simulation may be too coarse to realize the interpolation-correction with good accuracy; for example, *Nakajima and Nakajima* [1995] uses the angular steps of $\delta\theta_0 = 5°$, $\delta\varphi_v = 10°$, $\delta\theta_v = 5°$ to prepare their look-up tables

for the plane-parallel homogeneous retrieval scheme. As for the cloud parameter retrieval step itself, the present study extends and improves the one investigated in FIG01 in the more realistic conditions of the cloud parameter retrieval.

[81] We tested the whole retrieval procedure by preparing special radiance data set for flat-top bounded cascade cloud and flat-top and non-flat-top Gaussian process clouds. The cloud parameters of these inhomogeneous clouds could be retrieved with reasonable accuracy in spite of some discrepancies and large dispersions. The retrieved mean and standard deviation of optical thickness of the non-flat-top Gaussian cloud exhibits some dispersion; this implies that the variable cloud depth should be taken into account in the future development of retrieval procedure.

[82] Nevertheless, the present results tend to support the basic assumption that the exact type of 'direct' inhomogeneous cloud models is not important as far as the inhomogeneous clouds can be characterized by the first and second order moments of sub-pixel scale variances of cloud parameters. This assumption implies that one can neglect the effect of exact spatial distribution of fluctuations within an observation pixel as first approximation. However, these tests have been done only for the very limited conditions, and we have to continue such tests with bounded cascade, Gaussian process, and other clouds showing much larger range of parameter variations.

[83] We tried to answer a rather limited question, of how to use multiscale radiance data for the cloud parameter retrieval, and showed that the use of (0.25 km × 0.25 km) pixel radiance data could improve significantly the performance of the cloud parameter retrieval, especially the parameters associated with sub-pixel cloud inhomogeneity. This shows that the use of radiance data other than usual area-averaged multispectral radiance data may lead to the retrieval of more pertinent cloud parameters in addition to the usual optical thickness and effective radius. It should be remarked that the area-averaged data tend to be strongly correlated between them, and they provide only limited independent information content on a cloud parameter to retrieve. The measurement errors and/or approximations may smear out completely such limited information.

[84] An observation pixel of 1 km, used in the present study, is probably too small to neglect the effects of neighbor pixels on the target observation pixel even for a geometrical cloud depth of 0.3 km. It is noteworthy, however, that the present retrieval procedure can be applied to radiance data obtained for a larger observation pixel without any modification as far as the new target and input vectors share the same zone as those of 1 km pixel data in the corresponding vector spaces.

[85] It is quite evident that the present radiance database is too limited to cover the variability of cloud parameters of natural inhomogeneous clouds, since it comprises only 4 cloud scenes of 6.4 km × 6.4 km domain with constant geometrical cloud depth of 0.3 km and cloud base height of 0.5 km. Moreover, the cloud parameters in the present database exhibit high correlation, which would not be probably present in the natural cloud data. Appendix A and section 5 show that the assumption of the constant cloud depth induces a bias in the retrieved cloud parameters. Some of the discrepancies observed for Gaussian process cloud may probably occur because its cloud parameters and
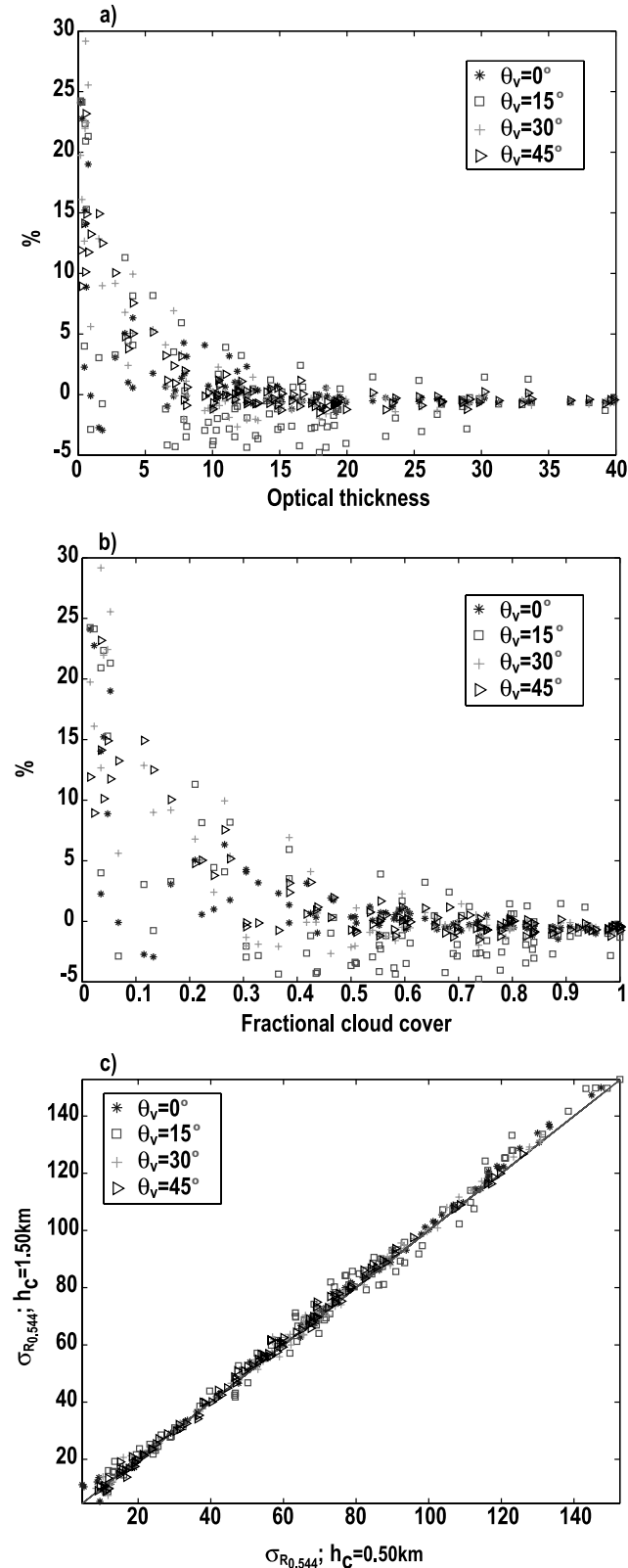
corresponding radiance data are outside the corresponding input vector space. These results raise many questions about the adequacy between the cloud parameters to retrieve and available radiance data, the statistical representativity of training data set, and the strategy of MNN training. We will discuss briefly some of these points which appear to be



**Figure A1.** Comparison of 0.544 μm radiance fields of bounded cascade inhomogeneous clouds with a geometrical cloud depth of 0.3 km but with two different cloud base heights of 0.5 km and 1.5 km respectively. The results are given for $\theta_0 = 30°$, $\varphi_v = 60°$ and $\theta_v = 0°$, 15°, 30°, and 45°. (a) Relative deviation of area-averaged radiance $R_{0.544}(h_c = 1.5$ km) with respect to $R_{0.544}(h_c = 0.5$ km) as a function of mean optical thickness. (b) Relative deviation of area-averaged radiance $R_{0.544}(h_c = 1.5$ km) with respect to $R_{0.544}(h_c = 0.5$ km) as a function of fractional cloud cover. (c) $\sigma_{R0.544}(h_c = 1.5$ km) as a function of $\sigma_{R0.544}(h_c = 0.5$ km).

critical for the development and improvement of the cloud parameter retrieval of inhomogeneous clouds.

[86] The first point is relative to the question about the adequacy between the cloud parameters to retrieve and available radiance data, i.e., what kind of radiance data is more pertinent for the planned cloud parameter retrieval, how to get additional independent informative radiance data, and how to define pertinent cloud parameters. The present study showed that the present MNN retrieval procedure which is based on the flat-top bounded cascade clouds could not manage to retrieve accurate mean and standard deviation of optical thickness. We have to test whether including non-flat-top cloud radiance data into the present training data set enables us to retrieve accurate mean optical thickness and standard deviation in addition to an 'effective' geometrical cloud depths, even if there is no guarantee that it is possible. On the contrary, the inclusion of inhomogeneous clouds with variable cloud depth and cloud base height requires necessarily additional data such as oxygen absorption band and/or thermal radiance at smaller pixels as input vector components. Otherwise, we may be probably retrieving more cloud parameters than the number of available radiance data.

[87] The second point, which is partly associated with the statistical representativity of database and training strategy, is to verify a basic implicit assumption that there is a one-to-one correspondence between target vector and input vector. The fact that all the necessary MNNs have been trained with acceptable generalization performance does not guarantee that multiple solution case does not occur for the inhomogeneous inverse cloud we have defined. To verify this assumption requires a 'target-input' database with a fine resolution both in target and input vector spaces; such database would also improve significantly the performance of MNNs. This also raises a question of how to choose an MNN training data set: a random sampling from all available radiance data or a uniform sampling in the input vector space. In the present study, we have opted to the random sampling because of the limited size of our radiance data, even if it is not a good solution to ensure a better approximation in a wider region of input data space.

[88] The third point is relative of what happens when we increase the number of desired cloud parameters and input vector components. As the dimension of target and input vector spaces increases, the main difficulty here is the phenomenon known as the 'curse of dimensionality' which implies the data sets of equal size become more and more spread out in both the target and input vector spaces. To realize a uniform sampling in the input space in such a

condition requires a radiance database much more extensive than the database we have prepared. However, we do not know expensive this radiance database should be; this means that we have to train MNNs for cloud parameter retrieval, and test and analyze them as we improve the radiance database. Anyhow, this preparation of a rather



expensive database seems to be inescapable; we have to work out an adequate strategy for radiance data simulation, including the development of more efficient radiative transfer codes. The second problem relative to the curse of dimensionality is how we train more efficiently the MNNs for the interpolation-correction and for the cloud parameter retrieval. We need to consider two problems: the one is how to avoid the training of an MNN for each incidence-viewing configuration and the second is how to choose an MNN with simpler structure. The first problem implies the development of new neural network training technique, and the second problem a better training strategy. What we have done in the present study is to use all available radiance data without eliminating any redundant data. The use of such input vectors results in a more complex MNN with too many hidden cells, while a better exploratory analysis would lead to an MNN with much simpler structure.

[89] Finally, one of the important limitations of the present study is that the radiance data used in the present study are 'monochromatic' radiance, while real satellite radiance data are weighted over a narrow band. Hence, to apply the present retrieval procedure to real data, we have to find a quick and precise method to convert narrow band weighted radiance to monochromatic radiance without doing new weighted radiance simulation. The quickest way to do this conversion is to train the MNNs for this data conversion even if such data conversion MNNs induce additional dispersions in retrieved cloud parameters. We have already trained and tested MNNs for such data conversion for the plane-parallel homogenous clouds, and intend to check the performance of these data conversion MNNs when they are applied to inhomogeneous clouds. Doing so would at least allow testing the performance of the present retrieval procedure with real satellite radiance data.

## Appendix A: Effects of Geometrical Cloud Characteristics on Area-Averaged Radiance and Standard Deviation of Radiance

[90] The radiance fields of inhomogeneous clouds with the same horizontal distribution of inhomogeneity may vary with the cloud base height and/or geometrical cloud depth. To evaluate these effects on the area-averaged radiance and standard deviation of radiance, we have simulated the radiance fields of an identical inhomogeneous cloud scene by changing the cloud base height and/or geometrical cloud depth.

[91] Figure A1 are for inhomogeneous clouds with a geometrical cloud depth of 0.3 km, but with two different
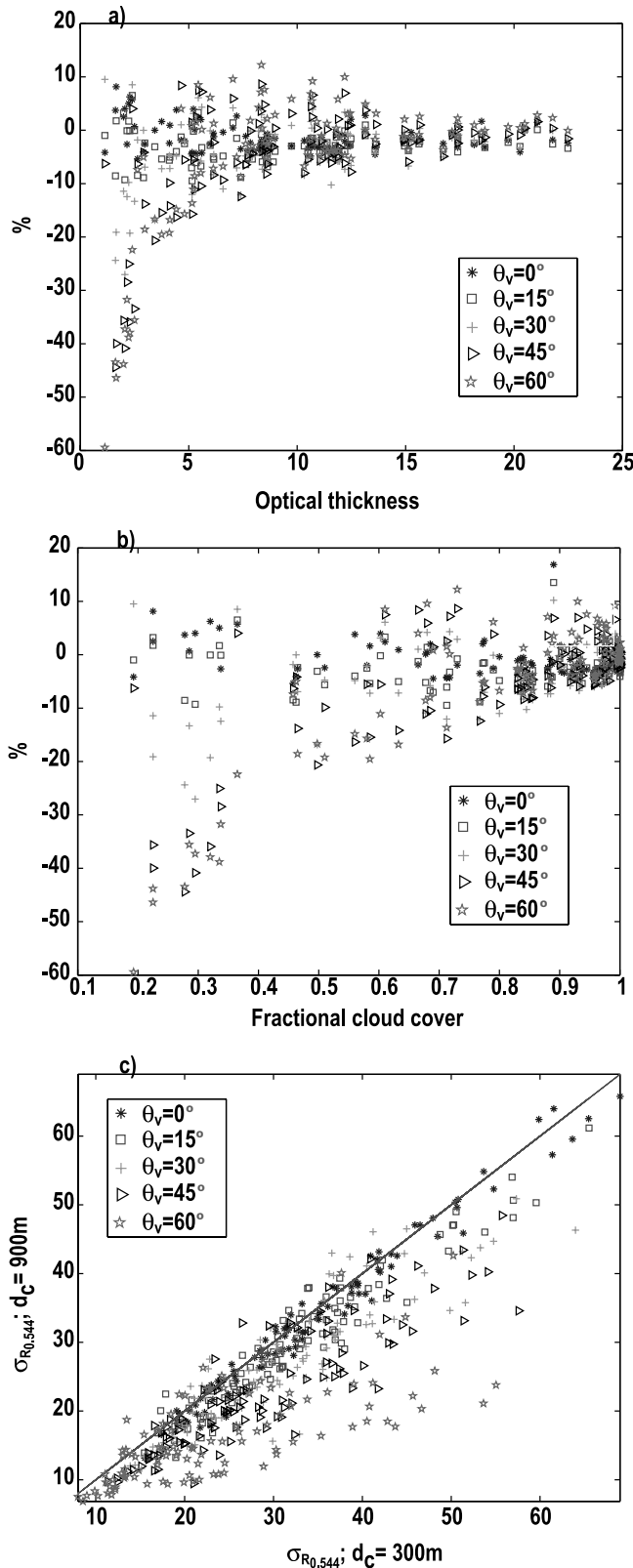
**Figure A2.** Comparison of 0.544 $\mu$m radiance fields of bounded cascade inhomogeneous clouds with a cloud base height of 0.5 km, but with 2 different geometrical cloud depths of 0.3 km and 0.9 km respectively. The results are given for $\theta_0 = 45°$, $\varphi_v = 60°$, and $\theta_v = 0°$, 15°, 30°, 45°, and 60°. (a) Relative deviation of area-averaged radiance $R_{0.544}(d_c = 0.9$ km$)$ with respect to $R_{0.544}(d_c = 0.3$ km$)$ as a function of mean optical thickness. (b) Relative deviation of area-averaged radiance $R_{0.544}(d_c = 0.9$ km$)$ with respect to $R_{0.544}(d_c = 0.3$ km$)$ as a function of fractional cloud cover. (c) $\sigma_{R0.544}(d_c = 0.9$ km$)$ as a fuction of $\sigma_{R0.544}(d_c = 0.3$ km$)$.

cloud base heights $h_c$ of 0.5 km and 1.5 km respectively; the domain cloud characteristics are ($\bar{\tau}_d = 15$, $\bar{r}_d = 20$ μm, $\bar{f}_d = 0.6$). The radiance fields were computed for a solar incidence angle of 30° and a surface albedo of 0.05. The area-averaged radiance $R_{0.544}$ and standard deviation $\sigma_{R0.544}$ were computed for randomly sampled observation pixels for different observation directions, and the results are plotted in Figure A1 for an observation direction of $\varphi_v = 60°$ and 4 different zenithal angles of $\theta_v = 0°$, 15°, 30°, and 45°. The relative deviation of the area-averaged radiance $R_{0.544}$ is plotted as a function of $\bar{\tau}_p$ (Figure A1a) and as a function of $\bar{f}_p$ (Figure A1b). The relative deviation of $R_{0.544}$ is defined by rel.dev. = $[R_{0.544}(h_c = 0.5$ km$) - R_{0.544}(h_c = 1.5$ km$)]/R_{0.544}(h_c = 0.5$ km$)$.

[92] The area-averaged radiance $R_{0.544}(h_c = 1.5$ km$)$ differs from $R_{0.544}(h_c = 0.5$ km$)$ by less than 3% for most of observation pixels with for moderate to large optical thickness ($10 < \bar{\tau}_p$), and the relative deviation decreases as $\bar{\tau}_p$ increases from 10 to 40 (Figure A1a). The relative deviation less than 5% corresponds to moderate to large fractional cloud cover ($0.4 < \bar{f}_p < 1.0$), and it decreases as $\bar{f}_p$ increases from 0.4 to 1.0 (Figure A1b). For $\bar{\tau}_p < 10$, the relative deviation is predominantly positive, and goes up to 30% for very small values of $\bar{\tau}_p$; these large relative deviations correspond mostly to small fractional cloud cover $\bar{f}_p < 0.4$. This feature is quite different from a quasi-symmetrical distribution of negative and positive deviations we would have expected. This may be because the solar radiation reflected from the underlying surface becomes more uniform and consequently smaller when the cloud base height is higher, which leads to the decrease of radiance upwelling from the cloud layer.

[93] Figure A1c shows that $\sigma_{R0.544}(h_c = 1.5$ km$)$ does not differ very much from $\sigma_{R0.544}(h_c = 0.5$ km$)$; the relative deviation of $\sigma_{R0.544}(h_c = 1.5$ km$)$ should remains the same order as those observed in Figure A1a. We also see that the dispersion of $\sigma_{R0.544}(h_c = 1.5$ km$)$ for $\theta_v = 15°$ are larger than for the other observation angles as in Figure A1a.

[94] Figures A2a, A2b, and A2c are the same as Figure A1, but for inhomogeneous clouds with a cloud base height of 0.5 km, but with two different geometrical depths $d_c$ 0.3 km and 0.9 km respectively; the domain cloud characteristics are ($\bar{\tau}_d = 10$, $\bar{r}_d = 12$ μm, $\bar{f}_d = 0.8$). The radiance fields were computed for both the clouds for a solar incidence angle of 45° and a surface albedo of 0.10.

[95] The relative deviation of $R_{0.544}(d_c = 90$ km$)$ is much larger than the relative deviation of $R_{0.544}(d_c = 1.0$ km$)$ observed in Figure A1. The area-averaged radiance $R_{0.544}(d_c = 0.9$ km$)$ differs from $R_{0.544}(d_c = 0.3$ km$)$ by less than 10% for ($10 < \bar{\tau}_p$), and the relative deviation decreases to less than 5% as $\bar{\tau}_p$ increases from 10 to 25 (Figure A2a). In Figure A2a, there is no apparent dependency of the relative deviation on the observation zenithal angle, except for small optical thickness $\bar{\tau}_p < 5$. The variation of relative deviation with the fractional cloud cover represented in Figure A2b differs significantly from that observed in Figure A1b. The relative deviation takes a value larger than 5% for a fractional cloud cover as large as 0.8 even if it tends to decrease with the fractional cloud cover (Figure A2b). There is a significant dependency of the relative deviation on the observation zenithal angle for small optical thickness.

[96] Figure A2c shows that $\sigma_{R0.544}(d_c = 0.9$ km$)$ differ significantly from $\sigma_{R0.544}(d_c = 0.3$ km$)$ and the former is frequently much smaller than the later. This underestimation is more evident for ($\theta_v = 45°$ and 60°) than ($\theta_v = 0°$ and 15°). Indeed, when the geometrical cloud depth increases while the horizontal distribution of cloudy and clear sky area are being kept unchanged, the aspect ratio of cloudy and clear sky area defined as (horizontal scale/vertical scale) decreases even if its fractional cloud cover viewed from the nadir remains identical. The direct solar radiation, especially for oblique solar incidence, has more chance to encounter cloud columns for geometrically deep clouds than for geometrically shallow clouds; this is also true for photons scattered by cloud columns, which tend to be more frequently intercepted by surrounding cloud columns. Consequently, inhomogeneous clouds with larger geometrical cloud depth tend to behave radiatively less inhomogeneous than inhomogeneous clouds with smaller geometrical cloud depth even if they have both the same horizontal distribution of cloud inhomogeneity and the same mean cloud domain optical thickness and effective radius.

[97] We may conclude that the variation of the cloud base height influences only slightly the area-average radiance $R_{0.544}$ and standard deviation $\sigma_{R0.544}$ for moderate to large optical thickness and for moderate to large fractional cloud cover, while the variation of the geometrical cloud depth has much larger effect on the area-average radiance $R_{0.544}$ and standard deviation $\sigma_{R0.544}$ even for moderate to large optical thickness and for moderate to large fractional cloud cover. Consequently, the cloud parameters retrieved with the present retrieval procedure may show some bias when the retrieval procedure is applied for inhomogeneous clouds with geometrical cloud depths much larger than 0.3 km because the present MNNs are trained with our present radiance database prepared with a constant geometrical cloud depth of 0.3 km.

## References

Barker, H. W., and J. A. Davies (1992), Cumulus cloud radiative properties and the characteristics of satellite radiance wavenumber spectra, *Remote Sens. Environ.*, *42*, 51–64.

Benassi, A., F. Szczap, A. Davis, M. Masbou, C. Cornet, and P. Bleuyard (2004), Thermal radiative fluxes through inhomogeneous cloud fields: A sensitivity study using a new stochastic cloud generator, *Atmos. Res.*, in press.

Brenguier, J. L., H. Pawlowska, L. Schüller, R. Preusker, J. Fischer, and Y. Fouquart (2000), Radiative properties of boundary layer clouds: Droplet effective radius versus number concentration, *J. Atmos. Sci.*, *57*, 803–821.

Cahalan, R. F., W. Ridgway, W. J. Wiscombe, T. L. Bell, and H. Harshvardhan (1994a), The albedo of fractal stratocumulus clouds, *J. Atmos. Sci.*, *51*, 2434–2455.

Cahalan, R. F., W. Ridgway, W. J. Wiscombe, S. Golmer, and H. Harshvardhan (1994b), Independent pixel and Monte-Carlo estimates of stratocumulus albedo, *J. Atmos. Sci.*, *51*, 3776–3790.

Cahalan, R. F., L. Oreopoulos, G. Wen, A. Marshak, T. C. Tsay, and T. DeFelice (2001), Cloud characterization and clear sky correction from Landsat 7, *Remote Sens. Environ.*, *78*, 83–98.

Chambers, L. H., B. A. Wielicki, and K. F. Evans (1997), Accuracy of the independent pixel approximation for satellite estimates of oceanic boundary layer cloud optical depth, *J. Geophys. Res.*, *102*, 1779–1794.

Coakley, J. A., and R. Davies (1986), The effect of cloud sides on reflected solar radiation as deduced from satellite observations, *J. Atmos. Sci.*, *43*, 1025–1035.

Davis, A., A. Marshak, R. F. Cahalan, and W. Wiscombe (1997), The Landsat scale break in stratocumulus as a three-dimensional radiative transfer effect: Implications for cloud remote sensing, *J. Atmos. Sci.*, *54*, 241–260.

Denison, D. G. T., C. C. Holmes, B. K. Mallick, and A. F. M. Smith (2002), *Bayesian Methods for Nonlinear Classification and Regression*, 277 pp., John Wiley, Hoboken, N. J.

Evans, K. F. (1998), The spherical harmonics discrete ordinate method for three-dimensional atmospheric radiative transfer, *J. Atmos. Sci.*, *55*, 429–446.

Faure, T., H. Isaka, and B. Guillemet (2001a), Neural network retrieval of cloud parameters of inhomogeneous and fractional clouds: Feasibility study, *Remote Sens. Environ.*, *77*, 123–138.

Faure, T., H. Isaka, and B. Guillemet (2001b), Neural network analysis of the radiative interaction between neighboring pixels in inhomogeneous clouds, *J. Geophys. Res.*, *106*, 14,465–14,484.

Faure, T., H. Isaka, and B. Guillemet (2001c), Mapping neural network computation of high-resolution radiant fluxes of inhomogeneous clouds, *J. Geophys. Res.*, *106*, 961–974.

Faure, T., H. Isaka, and B. Guillemet (2002), Neural network retrieval of cloud parameters from high-resolution multispectral radiometric data, *Remote Sens. Environ.*, *80*, 285–296.

Fu, Q., and K. N. Liou (1992), On the correlated k-distribution method for radiative transfer in nonhomogeneous atmospheres, *J. Atmos. Sci.*, *49*, 2139–2156.

Han, Q., W. B. Rossow, J. Chou, and R. M. Welch (1998), Global survey of the relationships of clouds albedo and liquid water path with droplet size using ISCCP, *J. Clim.*, *11*, 1516–1528.

Harris, C., X. Hong, and Q. Gan (1998), *Adaptive Modelling, Estimation and Fusion from Data: A Neurofuzzy Approach*, 323 pp., Springer-Verlag, New York.

Hecht-Nielsen, R. (1990), *Neurocomputing*, 433 pp., Addison-Wesley-Longman, Reading, Mass.

Iwabuchi, H. (2000), Effects of cloud horizontal inhomogeneity on optical remote sensing of clouds parameters, Ph.D. thesis, Univ. of Tohoku, Japan.

Iwabuchi, H., and T. Hayasaka (2002), Effects of cloud horizontal inhomogeneity on the optical thickness retrieved from moderate-resolution satellite data, *J. Atmos. Sci.*, *59*, 2227–2242.

Kaufman, Y. J., and T. Nakajima (1993), Effect of Amazon smoke on cloud microphysics and albedo-analysis from satellite imagery, *J. Appl. Meteorol.*, *32*, 729–744.

Kawamoto, K., T. Nakajima, and T. Y. Nakajima (2001), A global determination of cloud microphysics with AVHRR remote sensing, *J. Clim.*, *14*, 2054–2068.

Kneizys, F. X., E. P. Shettle, L. W. Arbeu, J. H. Chetwynd, G. P. Anderson, W. O. Gallery, J. E. A. Selby, and S. A. Clough (1988), *Users Guide to LOWTRAN-7*, Air Force Geophys. Lab. Tech. Rep. AFGL-TR-88-0177, 137 pp., Hanscomb, Mass.

Krasnopolsky, V. M., and H. Schiller (2003), Some neural network applications in environmental sciences. Part 1: Forward and inverse problems in geophysical remote measurements, *Neural Network.*, *16*, 321–334.

Legendre, P., and L. Legendre (1998), *Numerical Ecology*, 2nd ed., 853 pp., Elsevier Sci., New York.

Loeb, N. G., T. Varnai, and R. Davies (1997), Effect of cloud inhomogeneities on the solar zenith angle dependence of nadir reflectance, *J. Geophys. Res.*, *102*, 9387–9395.

Loeb, N. G., T. Varnai, and D. M. Winker (1998), Influence of sub-pixel scale cloud-top structure on reflectances from overcast stratiform cloud layers, *J. Atmos. Sci.*, *55*, 2960–2973.

Lucht, W., A. H. Hyman, A. H. Stralher, M. J. Barnsley, P. Hobson, and J. P. Muller (2000), A comparison of satellite-derived spectral albedos to ground-based broadband albedo measurements modeled to satellite spatial scale for a semi desert landscape, *Remote Sens. Environ.*, *74*, 85–98.

Mackay, D. J. C. (1992), A practical Bayesian framework for back-propagation networks, *Neural Comput.*, *4*, 448–472.

Marshak, A., A. Davis, W. Wiscombe, and G. Titov (1995), The verisimilitude of the independent pixel approximation used in cloud remote sensing, *Remote Sens. Environ.*, *52*, 71–78.

Marshak, A., A. Davis, R. Cahalan, and W. Wiscombe (1998), Non local independent pixel approximation: Direct and inverse problems, *IEEE Trans. Geosci. Remote Sens.*, *36*, 192–205.

Mayer, B. (1999), I3RC phase 1 results from the MYSTIC Monte Carlo model, Extended abstract for the *I3RC*, paper presented at Intercomparison of 3D radiation codes workshop, I3RC, Tucson, Ariz.

Nakajima, T., and M. D. King (1990), Determination of the optical thickness and effective particle radius of cloud from reflected solar radiation measurements. Part 1: Theory, *J. Atmos. Sci.*, *47*, 1878–1893.

Nakajima, T. Y., and T. Nakajima (1995), Wide-area determination of cloud microphysical properties from NOAA AVHRR measurements for FIRE and ASTEX regions, *J. Atmos. Sci.*, *52*, 4043–4059.

Nakajima, T., M. D. King, J. D. Spinhirne, and L. F. Radke (1991), Determination of the optical thickness and effective particle radius of cloud from reflected solar radiation measurements. Part 2: Marine stratocumulus observation, *J. Atmos. Sci.*, *48*, 728–750.

Neal, R. M. (1996), *Bayesian Learning for Neural Networks*, 210 pp., Springer-Verlag, New York.

Oreopoulos, L., and R. Davies (1998), Plane parallel albedo biases from satellite observations. Part I: Dependence on resolution and other factors, *J. Clim.*, *11*, 919–932.

Oreopoulos, L., A. Marshak, R. F. Cahalan, and G. Wen (2000a), Cloud three-dimensional effects evidenced in Landsat spatial power spectra and autocorrelation functions, *J. Geophys. Res.*, *105*, 14,777–14,788.

Oreopoulos, L., R. F. Cahalan, A. Marshak, and G. Wen (2000b), A new normalized difference cloud retrieval technique applied to Landsat Radiances over the Oklahoma ARM site, *J. Appl. Meteorol.*, *39*, 2305–2321.

Penny, W. D., D. Husmeier, and S. J. Roberts (1999), The Bayesian paradigm: Second generation neural computing, in *Artificial Neural Networks in Biomedicine*, edited by P. J. Lisboa, E. C. Ifeachor, and P. S. Szczepaniak, pp. 1–10, Springer-Verlag, New York.

Platnick, S., and F. P. J. Valero (1995), A validation of a satellite cloud retrieval during ASTEX, *J. Atmos. Sci.*, *52*, 2985–3001.

Roux, S. G., A. Arneodo, and N. Decoster (2000), A wavelet-based method for multifractal image analysis. III. Applications to high-resolution satellite images of cloud structure., *Eur. Phys. J. B.*, *15*, 739–764.

Szczap, F., H. Isaka, M. Saute, B. Guillemet, and A. Ioltukhovski (2000a), Effective radiative properties of bounded cascade nonabsorbing clouds: Definition of the equivalent homogeneous cloud approximation, *J. Geophys. Res.*, *105*, 20,617–20,634.

Szczap, F., H. Isaka, M. Saute, B. Guillemet, and A. Ioltukhovski (2000b), Effective radiative properties of bounded cascade absorbing clouds: Definition of an effective single-scattering albedo, *J. Geophys. Res.*, *105*, 20,635–20,648.

Varnai, T. (2000), Influence of three-dimensional radiative effects on the spatial distribution of shortwave cloud reflection, *J. Atmos. Sci.*, *57*, 216–222.

Varnai, T., and A. Marshak (2001), Statistical analysis of the uncertainties in cloud optical depth retrievals caused by three-dimensional radiative effects, *J. Atmos. Sci.*, *58*, 1540–1548.

Varnai, T., and A. Marshak (2002), Observations of three-dimensional radiative effects that influence MODIS cloud optical thickness retrievals, *J. Atmos. Sci.*, *59*, 1607–1618.

---

C. Cornet, Laboratoire d'Optique Atmosphérique, Université des Sciences et Technologies de Lille, F-59655 Villeneuve d'Ascq Cedex, France. (celine.cornet@loa.univ-lille1.fr)

B. Guillemet, H. Isaka, and F. Szczap, Laboratoire de Météorologie Physique, UMR/CNRS 6016, Université Blaise Pascal, F-63006 Clermont-Ferrand Cedex, France.